

## Fluid flow and heat transfer of porous TPMS architected heat sinks in free convection environment



Nada Baobaid<sup>a,b</sup>, Mohamed I. Ali<sup>a,b,d,\*1</sup>, Kamran A. Khan<sup>a,c</sup>, Rashid K. Abu Al-Rub<sup>a,b</sup>

<sup>a</sup> Advanced Digital & Additive Manufacturing Center, Khalifa University of Science and Technology, Abu Dhabi, United Arab Emirates

<sup>b</sup> Mechanical Engineering Department, Khalifa University of Science and Technology, Abu Dhabi, United Arab Emirates

<sup>c</sup> Aerospace Engineering Department, Khalifa University of Science and Technology, Abu Dhabi, United Arab Emirates

<sup>d</sup> Mechanical Power Engineering, Helwan University, Cairo, Egypt

### ARTICLE INFO

**Keywords:**

Heat sinks  
Cellular structures  
Triply periodic minimal surfaces  
Free convection  
Computational fluid dynamics

### ABSTRACT

Heat dissipation in electronic devices is challenging due its limited size and cooling space constraint. Implementing Triply Periodic Minimal Surfaces (TPMS)-based cellular structures could enhance the thermal exchange mechanism due to their novel architected, interconnected, and inter wind porous topologies and high surface area to volume ratio. In this study, three novel mathematically-driven TPMS heatsink structures were investigated using computational fluid dynamics (CFD) based models. TPMS heat sinks consisting of seven triply periodic unit cells were examined to investigate their thermal performance and fluid flow behavior in free convection air environment. The thermal performance indicators as convection heat transfer coefficient and surface temperature under parametric variation of applied heat load, fluid enclosure boundary condition, and TPMS structure orientation were determined. Enclosure boundary conditions found to have a significant effect on the thermal behavior of each heat sink structure; including radiation contribution was found to account for approximately 23% of the overall heat transfer in due to the complex TPMS internal structure. Three empirical Nusselt number correlations were then derived for the investigated TPMS structures. The results showed that TPMS-based heat sinks outperform conventional heat sinks by 48–61% owing to the random perturbations of flow and high packing density. This work shows the potential of TPMS porous architectures as very promising heat sinks.

### 1. Introduction

Nowadays, complex packing densities of heatsink have become prevalent in electronic devices. Heatsinks were studied for several decades to improve their configuration using conventional manufacturing methods. Heatsinks in many papers were studied using different fin's shapes, structures, and numbers to assess reaching higher heat dissipation. The conventional heat sinks often use extended fin surfaces, such as plate-fin [1–3], cylindrical fin heat sinks [3], cross-fin [4], pin-fin heat sinks [5,6], novel fin geometries heat sinks [7], micro-pin and plate-fin heat sinks [8,9], micro-channel heat sinks [10–13], etc. However, the commercially manufactured heat sinks have limitations in machining complex shapes when it comes to microscale; therefore, limiting the cooling

\* Corresponding author. Advanced Digital & Additive Manufacturing Center, Khalifa University of Science and Technology, Abu Dhabi, United Arab Emirates.

E-mail address: [mohamed.ali@ku.ac.ae](mailto:mohamed.ali@ku.ac.ae) (M.I. Ali).

<sup>1</sup> (Currently on Leave).

## Nomenclature

### Symbols

|                |  |
|----------------|--|
| $A$            | Area [ $m^2$ ]   |
| $c_p$          | Specific heat $[J/kg.K]$                               |
| $c$            | Kozeny Constant  |
| $Da$           | Darcy Number [-]                                       |
| $E$            | Total specific energy $[J/kg]$                         |
| $\mathbf{f}_b$ | Resultant of the body forces per unit volume $[N/m^3]$ |
| $g$            | Gravity $[m/s^2]$                                      |
| $h$            | Heat Transfer Coefficient $[W/m^2.K]$                  |
| $H$            | Total specific enthalpy $[J/kg]$                       |
| $I$            | 2nd-order identity tensor                              |
| $k$            | Thermal Conductivity $[W/m.K]$                         |
| $L$            | Height of the structure [m]                            |
| $Nu$           | Nusselt Number   |
| $Pr$           | Prandtl Number   |
| $\dot{q}$      | Heat load [W]  |
| $\ddot{q}$     | Heat flux $[W/m^2]$                                    |
| $Ra$           | Rayleigh Number  |
| $S$            | Energy Source $[J/m^3]$                                |
| $T$            | Temperature [ $K$ or $^\circ C$ ]                      |
| $\mathbf{T}$   | Viscous stress tensor $[N/m^3]$                        |
| $T_{RANS}$     | Reynolds stress tensor $[N/m^3]$                       |
| $t$            | Time (s)   |
| $v$            | Continuum velocity $[m/s]$                             |
| $\nabla$ .     | Divergence   |
| $\otimes$      | Tensor Product   |
| $\nabla$       | Gradient   |

### Greek Letters

|            |                                   |
|------------|-----------------------------------|
| $\alpha$   | thermal diffusivity $[m^2/s^2]$   |
| $\beta$    | Thermal Expansion $[1/K]$         |
| $\epsilon$ | Turbulent dissipation $[m^2/s^3]$ |
| $\kappa$   | Kinetic energy $[m^2/s^2]$        |
| $\lambda$  | Porosity [-]                      |
| $\mu$      | Dynamic viscosity $[N.s/m^2]$     |
| $\mu_t$    | Turbulent viscosity $[N.s/m^2]$   |
| $\nu$      | Kinematic Viscosity $[m^2/s]$     |
| $\rho$     | Density $[kg/m^3]$                |

*Subscript*

|               |                               |
|---------------|-------------------------------|
| <i>a</i>      | ambient                       |
| <i>convec</i> | Convection                    |
| <i>cond</i>   | Conduction                    |
| <i>e</i>      | Effective                     |
| <i>f</i>      | Fluid                         |
| <i>K</i>      | Permeability                  |
| <i>rad</i>    | Radiation                     |
| <i>s</i>      | Surface                       |
| <i>so</i>     | Solid                         |
| <i>sr</i>     | Surface with radiation effect |

*Superscript*

|   |                 |
|---|-----------------|
| — | Mean or Average |
|---|-----------------|

*Abbreviations*

|      |                                  |
|------|----------------------------------|
| TPMS | Triply Periodic Minimal Surfaces |
| CFD  | Computational Fluid mechanics    |
| SLM  | Selective Laser Melting          |

performance and occupying a large space. As a result, and due to the recent revolution in additive manufacturing (or commonly referred to by the industry as the 3D printing technology), researchers started to investigate complex geometries that were impossible to manufacture by conventional manufacturing methods. In comparison, cellular structures have complex geometries that induces tortuosity while occupying lower space. Cellular structures are a class of very porous structures where void spaces are integrated into their architecture. Arrangement of voids integrated into the cellular structures can be classified to be either periodic (*lattice structures*) or stochastic such as *foams* [14,15].

Many studies have been focused on integrating metal foams into thermal management applications [16–24]. Metals foams, regardless of their irregular inner morphology, possess a higher porosity leading to a lightweight structure and better fluid mixing phenomena compared to conventional heat sinks. Another motivation is the large surface area density and attractive stiffness properties [16]. Due to these significant advantages in the recent past, a focus on stochastic metals foams as heat sinks were studied. However, natural convection in metal foams literature is limited. Bhattacharya and Mahajan [17] experimentally examined natural convection of aluminum metal foam, showing a higher heat transfer coefficient of five to six times compared to the base plate heat sink. However, when compared to conventional heat sinks, the difference in heat transfer performance was found marginal. Furthermore, that study has shown that adding fins to the metal foam enhanced the heat transfer coefficient by 12–16% compared to the metal foam without fins and conventional heat sinks. Phanikumar and Mahajan [18] presented both numerical and experimental results of metal foams of different pore/void sizes, porosities, and base materials. The results showed that the Rayleigh number, thus, heat transfer mixing decreases as pore density increases. De Schampheleire et al. [19,20] and Billet et al. [21] experimentally and numerically analyzed the attribution of natural convection in Aluminum metal foams. Heat dissipation by conventional finned heat sinks was found to be three times higher than flat plate and two times higher than metal foams. The lower heat transfer of metal foam than pin-fin heat sinks explained by the higher hydraulic resistance of metal foams. Feng et al. [22] experimentally studied horizontally and vertically oriented metal foams with open slots, inspecting the relation of various geometries of different metal foam heights and foam strips widths. Qu et al. [23] experimentally showed a relation between the geometry of a horizontally copper metallic foam and thermal resistance. Zhao et al. [24] presented a combined numerical and experimental study of an open-cell metal foam. However, to thoroughly understand the fluid flow and heat transfer characteristics on metal foams is still a challenging task.

On the other hand, lattice structures have a periodic void distribution in 3D space with robust controllability of their interior geometry (i.e., architecture) compared to metal foams with stochastic structures. Furthermore, due to easiness in fabricating such lattice structures using various metallic additive manufacturing techniques, lately there has been an increasing interest in investigating the use of lattice structures as novel heat sinks especially due to their multifunctionality as compared to foam-based or conventional heat sinks. Ho et al. [25] experimentally investigated a new class of lattice structures (Rhombi-Octet) under forced convection. Four lattice structures were produced using the metal powder bed fusion additive manufacturing technique Selective Laser Melting (SLM). The lattice structures were found to have higher effective thermal conductivity and thermal efficiency index compared to metallic foams. However, the Nusselt number was observed to be less than metallic foams. The stochastic arrangement of void space in metallic foams enhances vortices and thus interfacial heat transfer rate compared to lattice structures. Tian et al. [26] have investigated diamond and square-shaped lattice structures and found that copper lattices exhibited higher thermal efficiency index compared to copper foam due to the lower pressure drop. Subsequently, Kim et al. [27] have described an experimental study on lattice structures subjected to forced convection. The vertices in the lattice structure were observed to increase heat transfer due to the formation of horseshoe vortices. Moreover, Chaudhari et al. [28] experimentally studied three octet-truss lattice structures manufactured using the SLM technique and found that the octet-truss lattices yield lower pressure drops and higher thermomechanical properties. Furthermore, Ekade et al. [29] characterized the fluid flow and thermal performance of octet-truss lattice compared to metal foam and found

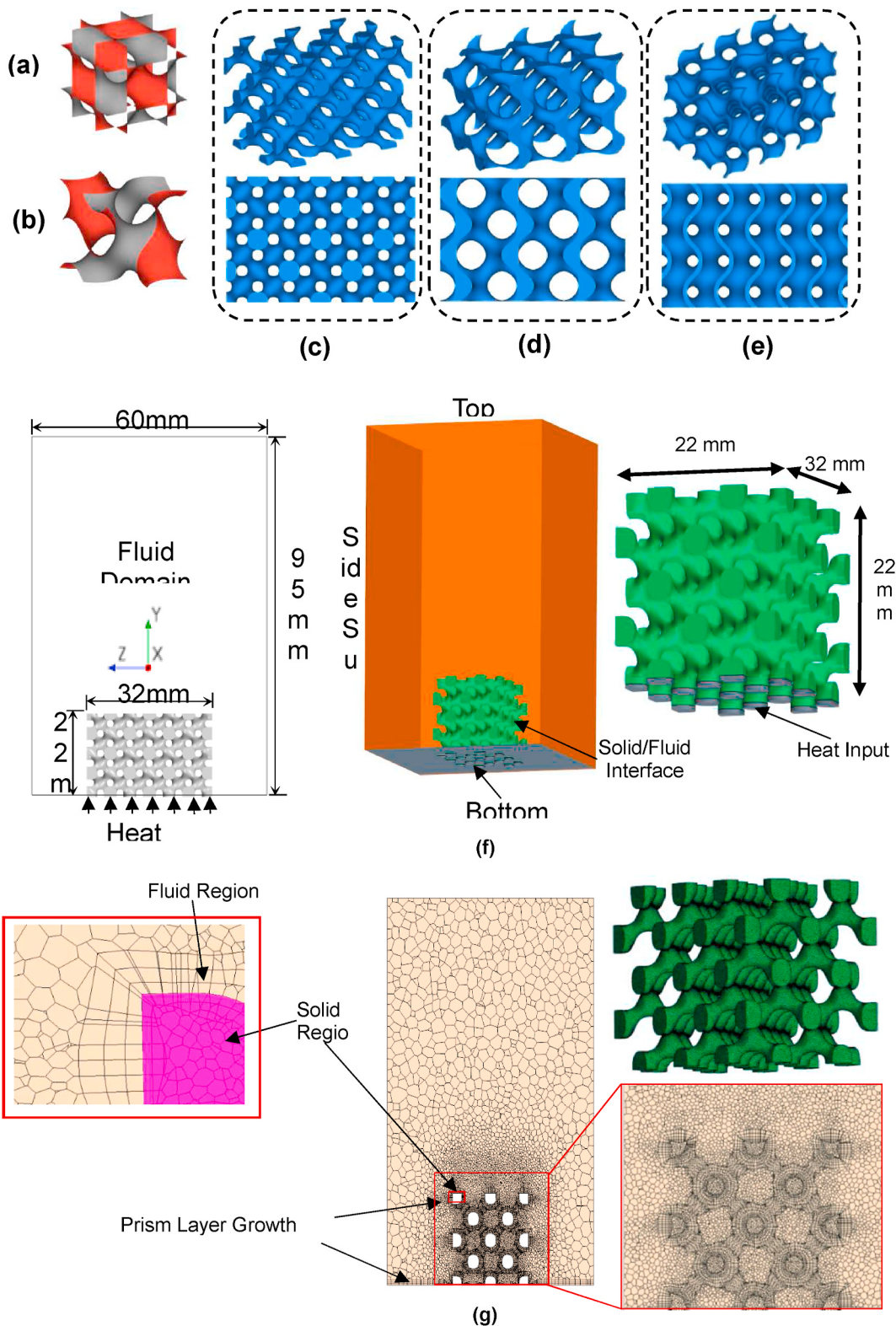


**Fig. 1.** One-unit cell of (a) Diamond and (b) Gyroid iso-surfaces, proposed heat sinks of (c) Diamond-Solid, (d) Gyroid-Solid and (e) Gyroid-Sheet showing both isometric (top) and side view (bottom), (f) computational domain of the heat sink and its environment, and (g) example of mesh distribution for the Diamond-Solid heat sink when sides and upper surfaces are open.

20–80% improved permeability; however, the thermal performance was similar for both lattice and metal foam, while the lattice has a lighter weight. Wen et al. [30] and Ozsipahi et al. [31] studied the thermal performance of anisotropic honeycomb lattice structures. Wang et al. [32] proposed a new design of a micro-latticed pin-fin heat sinks. In this study, cooling channels models with three different pin-fins: conventional solid square, vertex cubic lattice (VC), and body-centered cubic (BCC) lattice. Latticed pin-fin heat sinks contribute to lowering the pressure drop loss whereas BCC latticed pin-fin showed enhancement in the Nusselt number. TPMS novel heat exchangers, Gyroid structure and Schwarz-D structure, were studied to enhance heat transfer and improve the cycle efficiency of the supercritical carbon dioxide based Brayton cycle [33]. Despite all these studies on the thermal performance of lattice structures, these studies were done for forced convection cooling. One recent study, experimentally investigated the natural convection of a lattice structured heat sinks and compared with the conventional longitudinal fin solid heat sink [34]. Shamvedi et al. [34] 3D printed four heat sinks using the SLM additive manufacturing technique and compared one fin heat sink with three different lattice structures heat sinks. The thermal performance of the fin heat sink found to outperform the lattice structures, which was attributed to the lattice mesh structure that caused a higher pressure drop that negated the effect of higher surface area.

Lattice structures have been implemented as heat exchangers in some studies. Maloney et al. [35] constructed a cross-flow heat exchanger having a micro-lattice structure. Ho et al. [36] constructed heat exchangers made out of the previously investigated Rhombi-Octet structure while finding an increase in the air heat transfer coefficient. Son et al. [37] experimentally and numerically studied the lattice frame, compact heat exchangers. The lattice frame heat exchangers were found to have lower pressure drop compared to foams.

Lately, researchers have identified the best lattice topologies to obtain superior mechanical and physical behavior with consuming a lower amount of material with an increasing focus on mathematically defined architectures such as the triply periodic minimal surfaces (TPMS). TPMS have been found in nature as urchins, butterfly wings, and some liquid crystals [38]. In the year of 1866, Schwarz introduced the first TPMS structure named Primitive, after that several other TPMS structures have been introduced [39]. TPMS are complex 3D open-cell lattice topologies that have entangled surfaces and locally minimize the surface area of zero mean curvature [15,40]. The 3D periodic structure of TPMS topologies provides novel highly porous lattice structures, where pores are interconnected in 3D space with smooth surfaces with no geometric discontinuities [41]. Compared with other lattice structures, TPMS structures are more similar to natural structures without excessive connection joints where their architecture are more controlled than foam structures [42]. In fact, TPMS lattice structures are characterized by their smooth transition at the connection nodes as compared with the other types of truss-based cellular structures [15,43]. Moreover, TPMS are characterized by their high specific strength, permeability, and longer fatigue life [44]. Due to their properties, TPMS have been extensively investigated in many disciplines such as biomechanical and tissue engineering [43], high performance materials [45], porous scaffolds design [46], biomechanical meniscal implant [47], spacers and membranes for water treatment [49–51], structural engineering [42], catalytic supports [49], sound absorber [50] and heat and mass transfer [48,51–53]. TPMS-based lattice structures can be created either by thickening the minimal surface to create the sheet/shell-based lattice structures or by solidifying one of the internal volumes separated by the minimal surface to create the skeletal/ligament-based lattice structures [15]. Recently, Al-Ketan et al. [54] studied uniformly and functionally graded porosity TPMS heat sinks under forced convection and found them to be promising candidates for thermal management devices. Furthermore, Qureshi et al. [55–57] and Hu and Gong [58] have employed TPMS lattices for enhancing the thermal conductivity and heat transfer in phase change material in thermal energy storage and management systems. However, to our best knowledge, despite the novel geometric characteristics of TPMS lattices, their natural convection heat transfer characteristic have not been investigated as free convection heat sinks, which is the focus of the current study.

The fabrication of the geometrically complex periodic structures with superior mechanical and physical properties as TPMS-based lattices can be attained using various additive manufacturing (AM) techniques [59]. In these techniques, an energy source is used to create a 3D structure through a layer-by-layer method [15]. Several AM techniques can be used for fabricating metallic heat sinks such as, for example, selective laser sintering (SLS), selective laser melting, and electron beam melting (EBM) [14]. These techniques can process a range of metals including titanium, aluminum, steel, and copper alloys [14]. AM offers great flexibility in manufacturing heat sinks of complex geometries and more compact while avoiding high costs and leakage [60]. This technique has already been used for fabricating thermal management devices such as heat exchangers [36], heat sinks [34,61–65], boiling [66,67], and condensation [68].

The interest of implementing lattice structures with controlled topologies has been rising. TPMS, which can be mathematically designed, could be a novel alternative in designing and making high performing heat sinks. In this paper, thermal performance behavior and flow velocity of three TPMS-based heat sinks (Diamond-Solid, Gyroid-Solid and Gyroid-Sheet) either in solid-networks form or sheet/shell-network form are studied in natural convection under different enclosure types. In addition, Diamond-Solid and Gyroid-Sheet results were compared under different structure orientations. The influence of radiation into the three TPMS heat sinks was studied as well. This leads to thoroughly understanding the natural convection heat transfer characteristics of these novel heat sink designs.

## 2. Designs of TPMS-based heat SINKS

Heat transfer characterization and therefore thermal performance behavior of TPMS-based heat sinks as shown in Fig. 1 are investigated. Computational Fluid Dynamics (CFD) approach using Simcenter Star-CCM + platform is used in this study. TPMS structured heat sinks were mathematically generated and converted to CAD geometries using in-house developed MSLattice software [69]. Two promising TPMS geometries have been selected for the design of the proposed heat sinks that are: Diamond (Fig. 1(a)) and Gyroid (see Fig. 1(b)) that can be approximately described by the following level-set equations (Eq. (1) for the Gyroid and Eq. (2) for the Diamond):

$$\sin x \sin y \sin z + \sin x \cos y \cos z + \cos x \sin y \cos z + \cos x \cos y \sin z = C \quad (1)$$

$$\sin x \cos y + \sin y \cos z + \sin z \cos x = C \quad (2)$$

where  $x = 2\pi X/l$ ,  $y = 2\pi Y/l$ , and  $z = 2\pi Z/l$  with  $X$ ,  $Y$ , and  $Z$  are the Cartesian coordinates and  $l$  is the size of the unit-cell, and  $C$  is the level-set constant that controls the porosity of the heat sink.

In fact, as detailed by Al-Ketan et al. [15], TPMS-based lattices can be generated for a desired porosity as either in the form of solid-networks, where one of the two air volumes separated by the minimal surface are solidified, or in the form of sheet-networks, where the minimal surface which splits the air volume into two 50%/50% non-intersecting volumes is thickened. For comparison purposes, in this work the Gyroid TPMS is utilized to design both solid-network and sheet-network heat sinks; namely, Gyroid-Solid and Gyroid-Sheet (see Fig. 1(d) and (e)) whereas the Diamond TPMS is utilized as a solid-network heat sink; namely, Diamond-Solid (Fig. 1(c)). The 3D CAD geometries with a size of  $22 \times 32 \times 22$  mm are imported, surface cleaned, and meshed using the CFD platform remeshing tools. The selected TPMS heat sink porosity ( $\lambda$ ) is 0.80. The corresponding structure internal surface areas are  $92 \text{ cm}^2$  for the Gyroid-Sheet,  $44 \text{ cm}^2$  for the Gyroid-Solid and  $50 \text{ cm}^2$  for the Diamond-Solid. Therefore, the Gyroid-Sheet has more than double the surface area of the solid heat sinks, and the Diamond-Solid surface area is about 14% higher than the Gyroid-Solid surface area.

### 3. CFD modeling

In this work and as emphasized earlier, the CAD geometry of each proposed heat sink in Fig. 1 is imported to the Star-CCM + CFD platform where the surface cleaning and remeshing are performed for the solid and fluid regions. The interface between the solid and fluid regions, where the fluid boundary layer is taking place, is assigned as the heat transfer boundary between the heat sink solid and the fluid passing through the porous structure. The 3D TPMS heat sink CAD geometry is dipped in a 3D open environment of air that is used as a coolant for the heat sink. The environmental boundary conditions were considered as either walls or pressure outlet as it will be explained in more details in the procedure sections. Adapted CFD method with the meshing method, governing equations, considered parameters, physics setup, boundary conditions and temperature dependent fluid properties are detailed in the following subsections.

#### 3.1. Governing equations

In the finite volume method, Simcenter STAR-CCM + divides the domain into sub-domains and the equations are applied to each control volume. After applying the constitutive equations to the conservation equations, a closed-form is achieved. All conservation equations are written in terms of a generic transport equation in the software.

$$\underbrace{\frac{d}{dt} \int_V \rho \phi dV}_{\text{Transient Term}} + \underbrace{\int_A \rho v \phi \cdot da}_{\text{Convective Term}} = \underbrace{\int_A \Gamma \nabla \phi \cdot da}_{\text{Diffusive Term}} + \underbrace{\int_V S_\phi dV}_{\text{Source Term}} \quad (3)$$

Transient term accounts of the time rate of change of fluid property inside the control volume, convective and diffusive terms account for convection and diffusion across the boundaries and source term signifies the generation or destruction of fluid property inside the control volume. Where  $\phi$  is a scalar property as  $(1, u, v, w, E, H)$  and  $\Gamma$  is the diffusion coefficient.

Applying the appropriate values, special forms of mass, momentum and energy equations can be obtained. Mass, momentum and energy equations are applied for fluid domain and energy equation for solid domain.

The fluid flow equations undergo the assumptions of steady-state, Newtonian, incompressible flow, and ideal gas. No mass, momentum, or energy source is generated in the fluid during the simulation. Turbulence flow was chosen to account for any turbulence behavior. The fluid flow governing equations are shown as follows:

Mass Equation in Fluid:

$$\frac{\partial}{\partial t} \int_V \rho dV + \oint_A \rho v \cdot da = \int_V S_u \overset{\uparrow}{dV} \quad (4)$$

Momentum Equation in Fluid:

$$\frac{\partial}{\partial t} \int_V \rho v dV + \oint_A \rho v \otimes v \cdot da = - \oint_A p I \cdot da + \oint_A T \cdot da + \int_V f_b dV + \int_V S_u \overset{\uparrow}{dV} \quad (5)$$

Energy Equation in Fluids:

$$\frac{\partial}{\partial t} \int_V \rho E dV + \oint_A \rho H v \cdot da = - \oint_A \dot{q}'' \cdot da + \oint_A T \cdot v da + \int_V f_b \cdot v dV + \int_V S_u dV \quad (7)$$

Conduction      Viscous Work

The total energy is related to the total enthalpy  $H$  by:

$$E = H - p/\rho \quad (8)$$

where  $H = h + |\mathbf{v}|^2/2$  and  $h = c_p T$ . Where  $c_p$  is the specific heat capacity at constant pressure and  $T$  represents:

$$T = \mu (\nabla \bar{v} + (\nabla \bar{v})^T) - \frac{2}{3} (\mu \nabla \cdot \bar{v}) \mathbf{I} \quad (9)$$

$$T_{RANS} = \mu_t (\nabla \bar{v} + \nabla \bar{v}^T) - \frac{2}{3} (\mu_t \nabla \cdot \bar{v}) \mathbf{I} \quad (10)$$

For the enclosure of the Navier-Stokes equations, a suitable turbulence model must be chosen for the turbulent eddy viscosity  $\mu_t$  presented in Eq. (8). Reynolds-Averaged Navier-Stokes (RANS) turbulence model was used. In fact, there are two turbulence models in Star-CCM+ software; RANS turbulence model and Scale-resolving simulations. Even though the second turbulence model is more accurate, the first model gives a good approximation of the results and requires less computational time. For computing the eddy viscosity in the software, a  $\kappa$ - $\epsilon$  method was chosen with a two layers approach. The  $\kappa$ - $\epsilon$  model was chosen since it is suitable for complex recirculation. The Realizable  $\kappa$ - $\epsilon$  two layers approach was chosen to account for viscous affected layer near-wall in fine mesh regions. The  $\kappa$ - $\omega$  model can be used without requiring further modification, but it can be very sensitive to mesh near the walls. The two approaches were investigated and similar results were obtained. However, all the results reported through the study are based on the  $\kappa$ - $\epsilon$  and two-layer approach. The importance of activating the prism layer near the wall is significant in computing the flow behavior in the boundary layer region.

$$\mu_t = \rho C_\mu f_\mu \kappa t_{ts} \quad (11)$$

The  $C_\mu$  and  $f_\mu$  are the model coefficient and the damping function, respectively. For the Realizable  $\kappa$ - $\epsilon$  turbulence model with a two-layer approach chosen in this study, the turbulent time scale  $t_{ts}$  is calculated as  $t_{ets}$ :

$$t_{ets} = \frac{\kappa}{\epsilon} \quad (12)$$

The transport equations for the kinetic energy  $\kappa$  and turbulent dissipation rate  $\epsilon$  are given, respectively, as:

$$\nabla \cdot (\rho \kappa \bar{v}) = \nabla \cdot \left[ \left( \mu + \frac{\mu_t}{\sigma_\kappa} \right) \nabla \kappa \right] + P_\kappa - \rho \epsilon \quad (13)$$

$$\nabla \cdot (\rho \epsilon \bar{v}) = \nabla \cdot \left[ \left( \mu + \frac{\mu_t}{\sigma_\epsilon} \right) \nabla \epsilon \right] + \frac{1}{t_{ets}} C_{\epsilon 1} P_\epsilon - C_{\epsilon 2} f_2 \rho \frac{\epsilon}{t_{ets}} \quad (14)$$

where  $\sigma_\kappa$ ,  $\sigma_\epsilon$ ,  $C_{\epsilon 1}$  and  $C_{\epsilon 2}$  are the model coefficients,  $P_\kappa$  and  $P_\epsilon$  are production terms, and  $f_2$  is a damping function. Model coefficients, production terms and damping functions are specified for each type of the  $\kappa$ - $\epsilon$  model can be found in Ref. [70].

#### Energy Equation of solids:

For solid conductivity, the conduction of heat through the lattice structure was simulated using the heat diffusion equation Eq. (15). In solid, under steady-state and no generation of volumetric heat, the thermal diffusion equation can be written as.

$$\frac{d}{dt} \int_V \rho c_p T dV + \oint_A \rho e_p T v_s \cdot da = - \oint_A \dot{q}'' \cdot da + \int_V S_u dV \quad (15)$$

**Table 1**  
Mesh Sensitivity study for Diamond-Solid when top and sides are open.

| Base Size (mm) | Number of cells | Surface Temperature (°C) 0.5 W | Surface Temperature (°C) 2.1 W |
|----------------|-----------------|--------------------------------|--------------------------------|
| 50             | 52377           | 39.64                          | –                              |
| 40             | 427864          | 39.12                          | –                              |
| 30             | 777767          | 38.74                          | –                              |
| 25             | 1108265         | 38.89                          | 88.66                          |
| 22             | 1410189         | 38.97                          | 88.50                          |

where  $v_s$  is the solid convective velocity (Only for pure solid rotation).

Mass, momentum and energy sources are not included. Since  $\mathbf{f}_b$  accounts the body forces and in the following study gravity is the only body force acting in the model.

In the following study, the default second-order scheme was used to solve the flow. Besides this, computing gradient is required in numerical simulation to construct of variable value at the cell faces, secondary gradients for diffusion terms, pressure gradients calculations for pressure-velocity coupling, strain-rate and rotation-rate calculations for turbulence models.

Although the study was done upon steady-state analysis CFD solves the model as time steps until a quasi-steady state is achieved. The transient term is solved based on time steps with inner iterations in pseudo-time.

The coupled heat transfer between a fluid and a solid known as conjugate heat transfer (CHT). In CHT, energy equation for both solid the fluid domains are implicitly coupled and solved simultaneously at the fluid/solid interface. The mass and momentum equations are solved for the fluid only and on the solid/fluid interface, the energy transport as following:

$$T_{solid|_s} = T_{Fluid|_s} \quad (16)$$

$$\dot{q}_{solid|_s} = \dot{q}_{Fluid|_s} \quad (17)$$

$$-k \frac{\partial T_{solid}}{\partial n}|_s = h_f (T_s - T_{ref}) + \dot{q}_{rad} \quad (18)$$

### 3.2. Mesh study

#### 3.2.1. Mesh sensitivity for Diamond-Solid

The mesh properties defined at the continua of diamond solid are shown in [Table 1](#). The number of prism layers was chosen to be 3 instead of 2. The prism layer stretching is set to be 1.2, the prism layer stretching sets the growth rate of successive prism layers away from the wall. The prism layer thickness was set to be 5% of the base size, the default value is 33%. Choosing the prism layer thickness to be much smaller than the default to capture the behavior near the walls. The surface growth rate is chosen to be 1.2, the recommended growth rate is between 1.1 and 1.6 according to Ref. [71].

In the following table, [Table 1](#), the only changing parameter is the base size while all other parameters were kept constant. The interface mesh and boundary conditions were all fixed and the heat loads applied are 0.5 W and 2.1 W for the sensitivity study of choosing the base size.

Base size of 25 mm that produces 1.1 million cells was chosen based on the result of [Table 1](#). The chosen base size was selected based on both the values obtained and their convergence level. The dash line (—) represents an unconvvergence in the result.

In addition to the activate prism layer beside the walls, the prism layer was activated at the solid/fluid interface. A mesh sensitivity was applied to determine Prism layer surface size at the interface for 0.5W heat load as shown in [Table 2](#).

#### 3.2.2. Mesh Sensitivity for Gyroid-Solid and Gyroid-sheet

After that, the Gyroid-Solid structure [Table 3](#), 21 mm was chosen as a base size corresponding to 1.3 million cells. After this increase, the number of cells leads to unconvvergence of results. In Gyroid- Sheet structure, 24 mm was chosen as a base size corresponding to 1.6 million cells.

The same mesh sensitivity procedure was done for all cases of enclosures.

### 3.3. Computational procedure

The computational domain and geometry are shown in [Fig. 1\(f\)](#). TPMS heat sinks solid structures were immersed inside a fluid domain, atmospheric air at normal pressure and temperature (NTP) is used as the fluid domain. To avoid computational flow constraints, the fluid domain is created to be approximately 20 times larger than the heat sink. The distance between the solid and the fluid domain sides was equal in the x- and z-directions and the height is long enough to allow freedom of the fluid flow in the y-direction. The fluid domain control volume is surrounded by surface boundaries: top, bottom, and sides. These boundaries were either considered as *walls* or open to the atmosphere. As for executing the model, an extrusion of 0.5 mm at the bottom surface of the heat sink structures was introduced in order to act as a heater for imposing different heat loads and for examining the thermal performance of heat sinks.

The polyhedral mesh is used to generate mesh for solid and fluid regions as shown in [Fig. 1\(g\)](#). A conformal mesh is necessary, to achieve a mapped conformal mesh at the fluid/solid interface for ensuring the conjugate heat transfer mechanism. The mesh is clustered towards the solid zone using prism layer mesh. Using a fine prism layer assists in capturing the boundary layer phenomenon for the turbulence model that supports the viscous sublayer near the interface boundary. The prism layer stretching factor is set to be 1.2 such that this factor sets the growth rate of successive prism layers away from the interface wall towards the fluid region.

**Table 2**

Mesh sensitivity of prism layer surface size at solid/fluid interface.

| Prism Layer size (% of base size) | Surface Temperature (°C) |
|-----------------------------------|--------------------------|
| 15–25                             | 39.77                    |
| 3–10                              | 39.03                    |
| 1–5                               | 37.60                    |
| 0.5–4.5                           | 37.90                    |

**Table 3**

Mesh Sensitivity Study for Gyroid-solid when top and sides are open.

| Base Size (mm) | Number of cells | Surface Temperature (°C) 0.5 W | Surface Temperature (°C) 2.1 W |
|----------------|-----------------|--------------------------------|--------------------------------|
| 23             | 1140681         | 41.40                          | –                              |
| 22             | 1219499         | 40.59                          | 79.62                          |
| 21             | 1360331         | 40.38                          | 86.5                           |
| 20             | 1413443         | 40.40                          | 79.40                          |

**Table 4**

Mesh Sensitivity Study for Gyroid-sheet when top and sides are open.

| Base Size (mm) | Number of cells | Surface Temperature (°C) 0.5 W | Surface Temperature (°C) 2.1 W |
|----------------|-----------------|--------------------------------|--------------------------------|
| 30             | 1132277         | –                              | –                              |
| 28             | 1698800         | –                              | –                              |
| 24             | 1857444         | 41.3                           | 96.21                          |
| 23             | 2046119         | 41.4                           | 96.08                          |

**Table 5**

Chemical composition and thermal properties of the AlSi10Mg.

| Chemical Composition in wt.%         |            |                   |                   |                   |   |                   |                  |                   |                   |                   |  |
|--------------------------------------|------------|-------------------|-------------------|-------------------|---|-------------------|------------------|-------------------|-------------------|-------------------|--|
| Al<br>balance                        | Si<br>9–11 | Fe<br>$\leq 0.55$ | Cu<br>$\leq 0.05$ | Mn<br>$\leq 0.45$ | Mg<br>0.2–0.45                                  | Ni<br>$\leq 0.05$ | Zi<br>$\leq 0.1$ | Pb<br>$\leq 0.05$ | Sn<br>$\leq 0.05$ | Ti<br>$\leq 0.15$ |  |
| Thermal Properties ( $T$ unit is °C) |            |                   |                   |                   |   |                   |                  |                   |                   |                   |  |
| Density (kg/m <sup>3</sup> )         |            |                   |                   |                   | $\rho = -0.2 T + 2690.3$                        |                   |                  |                   |                   |                   |  |
| Specific heat (J/kg.K)               |            |                   |                   |                   | $c_p = 0.001 T^2 - 0.03 T + 900.7$              |                   |                  |                   |                   |                   |  |
| Conductivity (W/m.K)                 |            |                   |                   |                   | $k = -8 \times 10^{-5} T^2 - 0.0395 T + 196.65$ |                   |                  |                   |                   |                   |  |

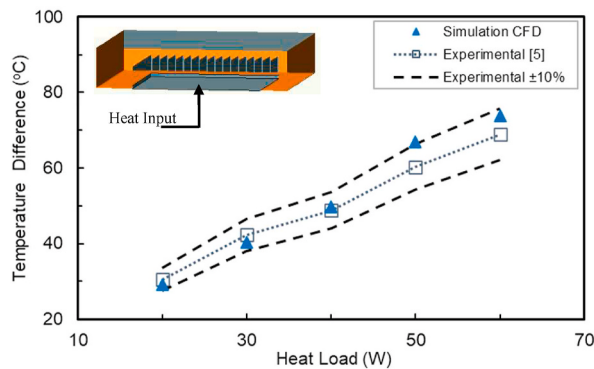


Fig. 2. CFD validation against plate-fin heat sink showing comparison between experimental [5] and current CFD numerical results.

Customized mesh cells and properties were achieved based on each geometry and the associated boundary conditions until satisfying converged results are obtained. In Fig. 1(g) as sides and top surface are opened the prism layer was generated at the bottom of enclosure only. The influence of mesh was tested for two different heat loads to ensure the mesh objectivity of the results. The results were assumed to be converged when the calculation residuals of energy and fluid flow properties reach their minimum values and show no more change in their values during the simulations.

TPMS heat sinks energy equation is solved in a coupled manner with the fluid energy at the interface with no-slip boundary condition imposed on the solid surfaces. The governing equations is solved simultaneously using a coupled solver discretized using a second-order upward scheme for convective flux and second-order central difference for diffusive flux. The coupled system of equations is solved by an implicit time-integration scheme. For surfaces specified as walls in the air control volume, a smooth, adiabatic, and no-slip wall conditions are assumed. However, for surfaces specified as a *pressure outlet*, the surface is exposed to the surrounding, boundary pressure is considered as the pressure of the environment, and the temperature was set to 25 °C. The base material of the heat sink is selected as the aluminum alloy AlSi10Mg, which is a widely used 3D printable material using the powder bed fusion additive manufacturing technique, where its chemical composition is shown in Table 5 and its thermal properties were curve-fitted after obtaining them using JMATPro software [72]. On the other hand, the ideal gas model is used for the air density and polynomial temperature dependence functions are used for the rest of the fluid properties.

#### 4. Results and discussion

CFD modeling verification and validation results followed by the parametric study results for the three TPMS heat sink geometries are presented in the following subsections. Flow velocity and temperature contours are presented and thoroughly discussed to explain the heat transfer performance of the investigate heat sinks. Empirical correlations have been developed using the current results.

##### 4.1. Validation

For the model validation study, the experimental results of a typical compact heat sink investigated in Ref. [5] were compared with CFD simulation results (see Fig. 2). The conduction effect within the heat sink was neglected, convection and radiation were considered. The sides were chosen to be open to the atmospheric pressure in the simulation to conform the experimental setup. The emissivity of the sides considered to be unity as the surrounding was assumed to absorb all the incoming radiation. The bottom surface was chosen to be open as well to account for the space between the bottom plate and the bottom surface of the heat sink -insulation foam space-which is shown in the experimental setup. The top surface which is Perspex, emissivity was chosen to be 0.86 [73] and wall selected to be transmitting. The top surface boundary condition is chosen to be environmental. Having environmental condition, the outer surface of the top plate is considered to be cooled by natural convection having a heat transfer coefficient of 5.65 W/m<sup>2</sup>.K. The heat transfer coefficient was obtained from Table 2. The comparison between the experimental and CFD computational results is

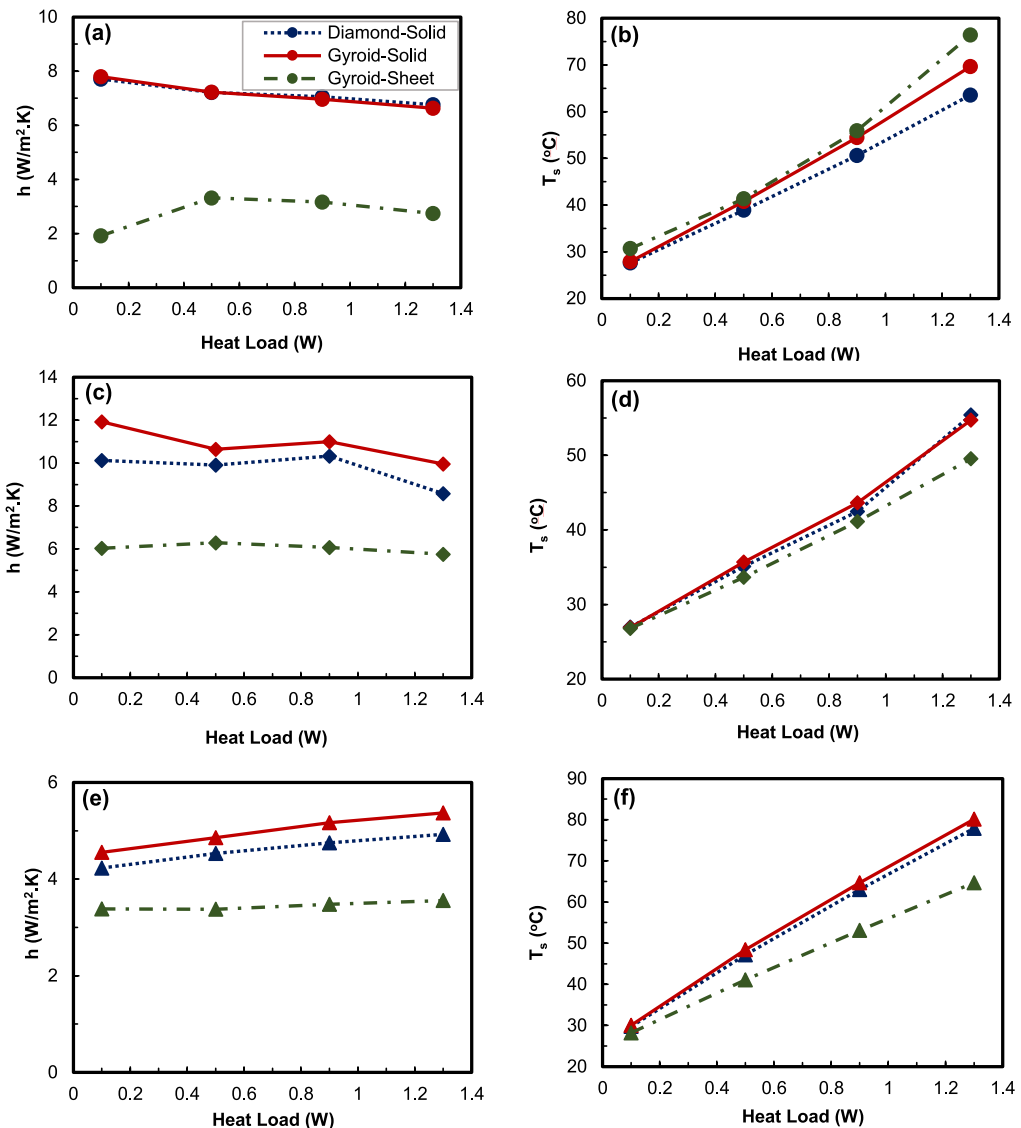


**Fig. 3.** Heat transfer coefficient [(a), (c), (e)] and surface temperature [(b), (d), (f)] of TPMS-based heat sinks for three boundary conditions: (a)–(b) top and sides are open, (c)–(d) top and bottom surfaces are open and (e)–(f) bottom surface is open.

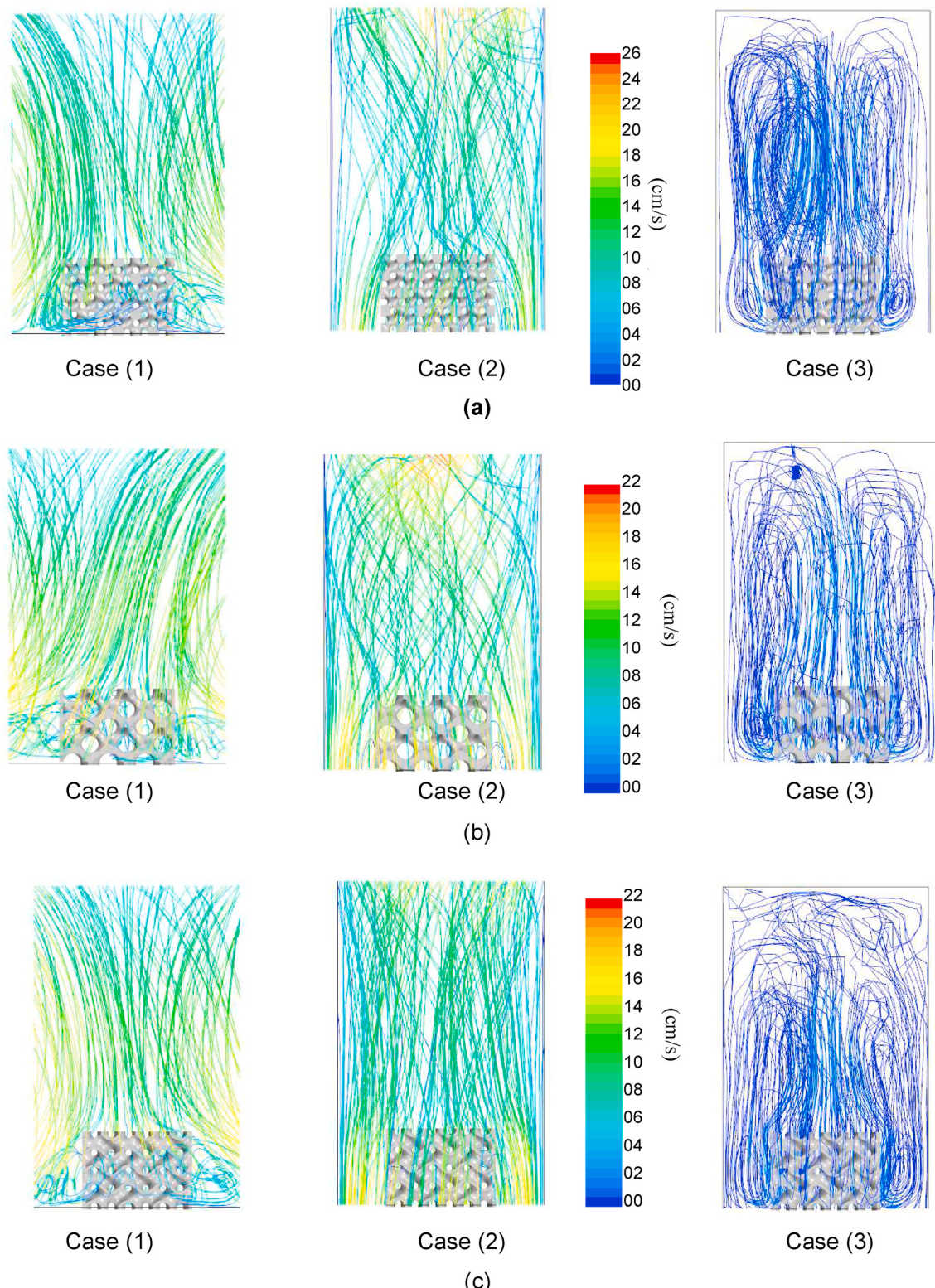


**Fig. 4.** Velocity streamline flow of (a) Diamond-Solid, (b) Gyroid-Solid and (c) Gyroid-Sheet heat sinks for the three enclosure boundary conditions; Case (1): top and sides are open, Case (2): top and bottom are open, and Case (3): bottom surface is open.

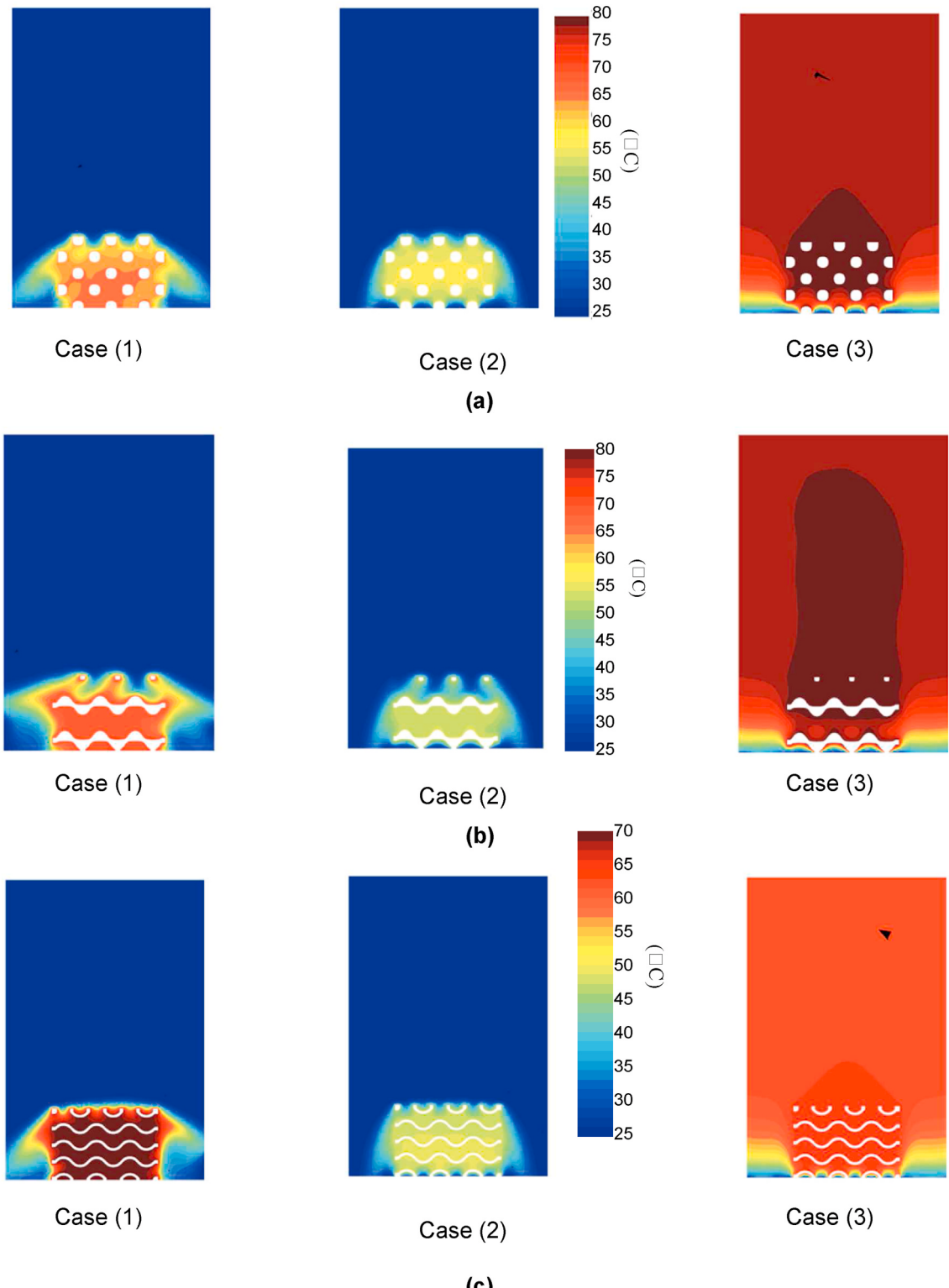


**Fig. 5.** Temperature contour of (a) Diamond-Solid, (b) Gyroid- Solid and (c) Gyroid-Sheet heat sinks for the three enclosure boundary conditions; Case (1): top and sides are open, Case (2): top and bottom are open, and Case (3): bottom surface is open.

exploited in Fig. 2 for the temperature difference between the solid surface and fluid versus the heat load. The overall results showed an agreement within  $\pm 10\%$  experimental uncertainty, a slight overestimation occurs with increasing the heat load; however, it is still within the  $\pm 10\%$  difference.

#### 4.2. Effect of the TPMS heat sink design parameters

In total forty-four CFD simulations were carried out to observe the effect of boundary conditions and heat sink's orientation on the thermal performance and flow behavior of the proposed TPMS-based heat sinks excluding the radiation effect. The thermal performance indicators are the average surface temperature and the average heat transfer coefficient  $\bar{h}$ , which was obtained as:

$$\bar{h} = \frac{\dot{q}}{A_s(T_s - T_a)} \quad (19)$$

where  $\dot{q}$  is the heat transfer from the interface,  $A_s$  is the interfacial surface area,  $T_s$  is the surface temperature and  $T_a$  is the ambient temperature.

##### 4.2.1. Effect of enclosure boundary conditions

Three enclosure boundary conditions were examined through this section:

*Case (1):* Exposing top and sides surfaces of the enclosure to the surrounding, Fig. 3(a)-(b).

*Case (2):* Exposing top and bottom surfaces of the enclosure to the surrounding, Fig. 3(c)-(d).

*Case (3):* Exposing bottom surfaces of the enclosure to the surrounding, Fig. 3(e)-(f).

Having different enclosure types can affect the velocity flow lines; thus, affecting the thermal behavior of the heat sinks.

**4.2.1.1. Heat transfer coefficient and surface temperature.** The heat transfer coefficient and the surface temperature obtained for the TPMS heat sinks are presented in Fig. 3 for the three enclosure boundary conditions as a function of heat load. Fig. 3(a) shows a slight drop in the heat transfer coefficient for the Diamond-Solid and Gyroid-Solid heat sinks when the top and sides are opened (i.e., Case (a)) to the surrounding. Both Solid-type heat sinks have almost similar trends and results of the heat transfer coefficient. Fig. 3(b) shows that the surface temperature of Diamond-Solid for Case (a) is the lowest among the TPMS heat sinks, which indicates the best thermal performance. The better performance of Diamond-Solid compared to Gyroid-Solid is explained by the slight increase in its surface area. However, the difference between the surface temperature of Solid-based heat sinks is around 1%-10% which indicates that the difference in thermal performance in both heat sinks is marginal for all cases (compare Fig. 3(b), (d), and (f)). On the other hand, the Gyroid-Sheet heat sink, according to Fig. 3(a), has significantly lower heat transfer coefficient, whereas its surface temperature (Fig. 3(b)) reaches 18% higher than Solid-based heat sinks at 1.3 W. This explained by the high surface area of the Gyroid-Sheet heat sink which is approximately twice the surface area of Solid-based heat sinks. The relatively larger surface area and complex geometry of the Gyroid-Sheet heat sink tend to block the flow. Increasing heat load between 0.1 W and 0.5 W leads to an increase of heat transfer coefficient due to the larger surface area which starts to act as a barrier to the flow. Fig. 3(c) for Case (2) shows that the heat transfer coefficient of Diamond-Solid heat sink is approximated to be  $10 \text{ W/m}^2\text{K}$  between 0.1 and 0.9 W heat loads. Increasing the heat load from 0.9 to 1.3 W leads to a noticeable drop in heat transfer coefficient for the Solid-based heat sinks. Fig. 3(c) shows that the Gyroid-Sheet for Case (2) has an approximate heat transfer coefficient of  $6 \text{ W/m}^2\text{K}$  for all heat loads. Referring to the surface temperature between 0.1 and 0.9 W, the three structures are showing an almost similar trend of surface temperature with the Gyroid-Sheet is slightly lower than the Solid heat sinks (Fig. 3(d)). However, between 0.9 and 1.3 W the Solid structures' surface temperature starts diverging from the Gyroid-Sheet value to have an almost 11% difference at 1.3 W. This is explained by the drop of heat transfer coefficient of Solid structures at this range. In addition, Fig. 3(e), which represents the thermal performance for Case (3), shows a slight increase of heat transfer coefficient of the Solid-based TPMS structures as heat load is increasing, and an almost constant value for

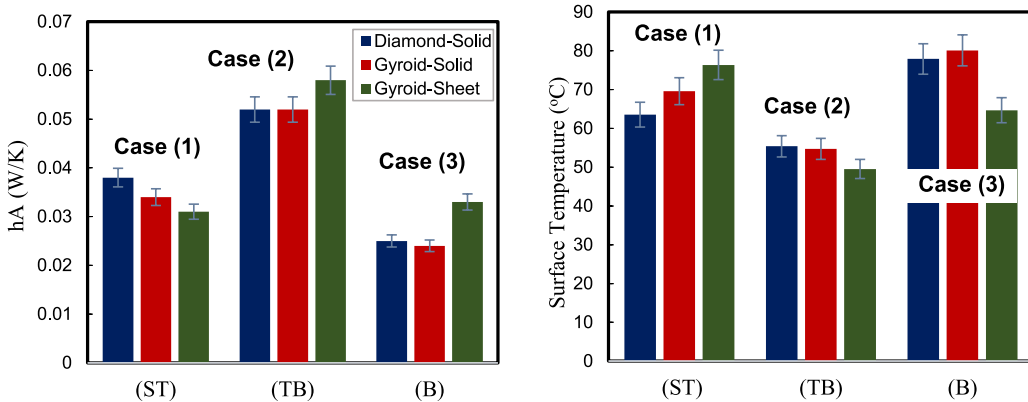


**Fig. 6.** (a) Maximum areal heat transfer coefficient and (b) maximum surface temperature of the proposed TPMS-based heat sinks under the three enclosure boundary conditions; Case (1): top and sides are open, Case (2): top and bottom are open, and Case (3): bottom surface is open.

Gyroid-sheet. Fig. 3(f) shows that the surface temperature values of Solid-based heat sinks are almost the same. Gyroid-Sheet heat sink yields better performance compared to solid structures when the bottom surface is open, Case (3), as the surface temperature is 21% lower than the Solid-based heat sinks (see Fig. 3(f)). However, Case (2) boundary condition configuration is the best for the three TPMS structures.

**4.2.1.2. Velocity and temperature contours.** Fig. 4 shows the flow streams and flow velocity contours for Diamond-Solid, Gyroid-Solid and Gyroid-Sheet. These results are illustrated for the three assumed different enclosure surrounding boundary conditions (i.e., Cases (1), (2), and (3)). As it can be seen in all figures that the surrounding boundary constrain conditions significantly affect the flow stream direction and velocity magnitude. Opening the top and bottom boundary, Case (2), while the sides are closed showed the best

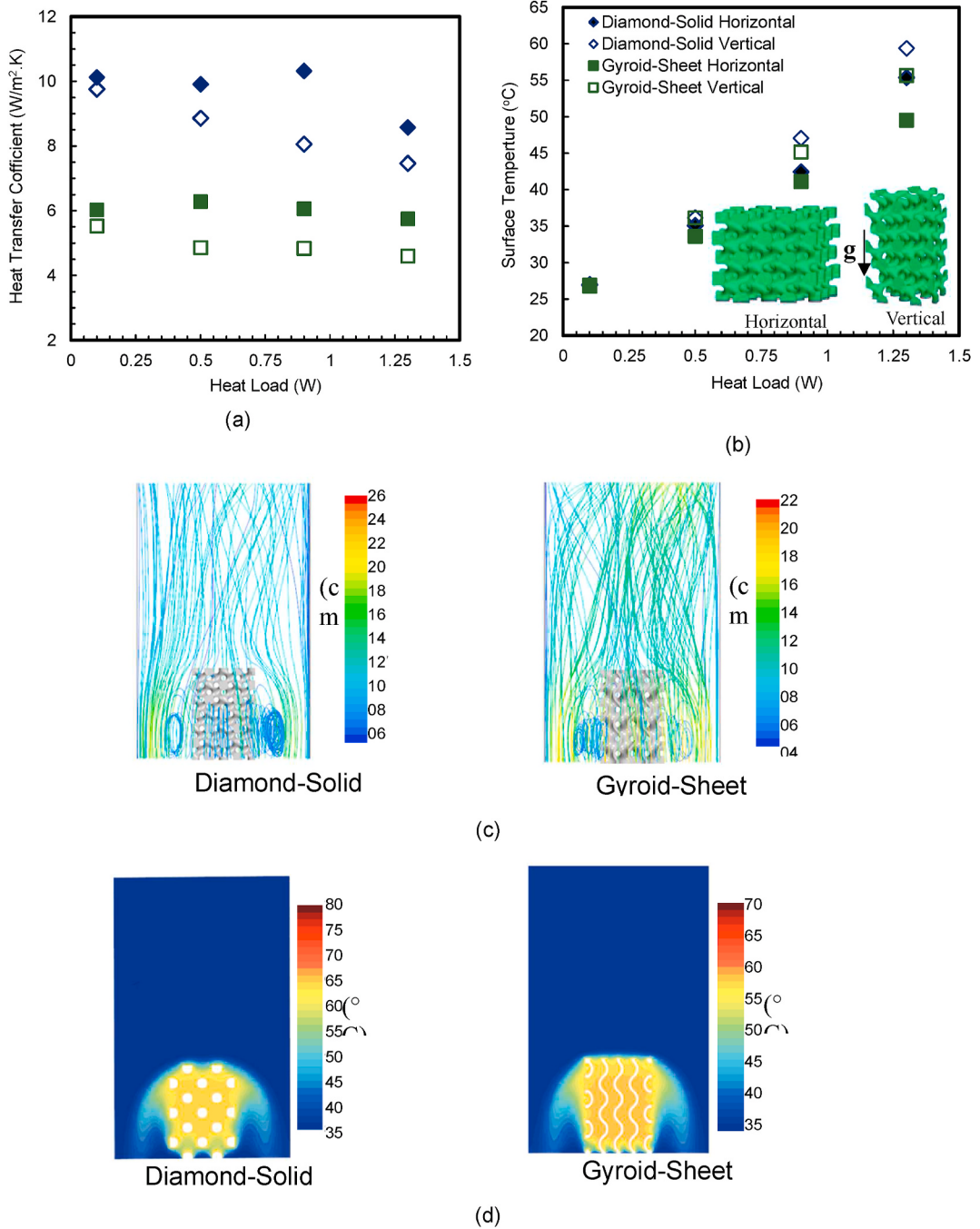


Fig. 7. Effect of Diamond-Solid and Gyroid-Sheet horizontal and vertical orientations under Case (2) on (a) heat transfer coefficient and (b) surface temperature. (c) Velocity streamline flow and (d) temperature contours for the vertically oriented Diamond-Solid and Gyroid-Sheet TPMS-based heat sinks.

streamlines alignment compared to the other two configurations; Cases (1) and (3). This setup leads to the best cooling performance as can be seen from the TPMS surface temperature contours in Fig. 5 for Case (2). When either the top or the bottom boundaries are closed, the flow streams are crossing each other and generating a vortices on the sides of the TPMS that is mixing the hot and cold cooling air streams causing a reduction in the convection heat transfer coefficient and therefore an inefficient cooling. The results of that inefficient cooling in translated to a higher TPMS surface temperature as it can be seen in Fig. 5 for Case (2). The worst-case scenario is when the top and sides are constrained by closed boundaries while only the bottom is opened (i.e., Case (3)). It showed a very complex turbulent flow associated with vortices and; therefore, a significant mixing between the hot and cold air that could cause the cooling air to reach a thermal equilibrium condition with the TPMS surface temperature. Interestingly, it is noted in the case of the Gyroid-Sheet heat sink, the highest temperature of the solid surface is obtained when the bottom boundary is closed while the top and side boundaries are open (i.e., Case (1)). This observation can be justified by looking at the nature of the TPMS Gyroid sheet-networks that have relatively much smaller flow passages due to its sheet/shell geometry. The pressure drop resistance in these relatively narrow passages will be defeated by the fluid flow momentum from the bottom to the top due to the buoyancy effect; however, it will be so difficult to get through the passages from the sides due to the significant resistance from the pressure losses across the passages in the absence of fluid flow momentum. Therefore, in Fig. 4 (c), Case (1), due the complex topology and lower permeability of the Gyroid-Sheet heat sink, surrounding air flow is facing a significant resistance to enter the structure leading to an accumulation of hot air inside the heat sink.

Since the bouncy force is the prime-mover of the free convection heat transfer, it has been shown through the current simulations that the top and bottom opening boundary condition, Case (2), is the best for uniform flow and; therefore, the efficient heat sink cooling performance. However, most of the heat sink applications require that the heat sink bottom to be attached to the hot surface that needs to be cooled. Therefore, forced convection is mandatory to force the cooling air from the sides of the TPMS structures when the cooling load cannot be removed by natural convection. Maximum heat transfer rate and maximum surface temperature for the three TPMS structures is illustrated in Fig. 6(a) and (b), which depicts the significance of the internal structure, both surface area and permeability, on the heat transfer performance. Therefore, the results in Fig. 6(a) and (b) describe the TPMS-based heat sink heat transfer coefficient times the heat sink surface area ( $hA$ ) and average surface temperature, respectively. Moreover, Fig. 6(a) and (b) show that the current Solid-based TPMS heat sinks do not have a significant difference in temperature and overall heat transfer coefficient (i.e., areal heat transfer coefficient) ( $hA$ ). On the other hand, the current Sheet-based TPMS Gyroid heat sink shows noticeable improvements in the overall heat transfer coefficient and surface temperature when the bottom boundary is opened (i.e., Case (3)) due to the nature of its vertical passages and relatively larger surface area density. Therefore, the enclosure's boundary constraint is an important factor that can have a significant impact on the heat sink performance.

#### 4.2.2. Effect of the heat sink orientation

TPMS-based heat sink orientation is studied in this section as shown in Fig. 7(a) and (b) under opening the top and bottom surfaces; Case (2). Investigating the effect of orienting of Diamond-Solid and Gyroid-Sheet heat sinks  $90^\circ$  around the x-axis versus the already investigated horizontal orientation on the heat transfer coefficient and surface temperature are shown in Fig. 7(c) and (d). The heat transfer coefficient is shown to be decremented under vertical orientation, where the 32 mm long side is aligned with the vertical direction. The thermal performance of Diamond-Solid is 7% more efficient in the horizontal orientation, where the 32 mm long side is aligned with the horizontal direction, based on their highest heat load. For the Gyroid-Sheet heat sink, thermal performance is found to be 11.5% more efficient in the horizontal orientation.

Having the longest side of the heat sink in the vertical direction leads to enhanced buoyancy force. However, the increase of the buoyancy force was concurred by the increase of flow resistance due to the vortex generated flow on the sides of the structure as shown in Fig. 7(c). The longer vertical side will also create a thicker hydrodynamic and thermal boundary layers around and inside the heat sink as the boundary layer thickness increases in the direction of the flow. Therefore, the boundary layer inside the heat sink will grow as well as the boundary layer around the heat sink causing the dominance of molecular diffusive heat transfer mode over the convective mode inside the structure and growing the vortex flow around it. In addition, when the longer side is in the flow direction, this will lead the hot air molecules to travel through the longer distance resulting in reducing the overall thermal performance and

**Table 6**  
Thermal radiation contribution in the proposed TPMS-based heat sinks.

| Heat sink type | Total Heat Dissipation (W) | Heat Dissipation by convection + conduction (W) $\dot{q}_{\text{conv+cond}}$ | Heat Dissipation by Radiation (W) $\dot{q}_{\text{rad}}$ | Radiation Contribution (%) |
|----------------|----------------------------|--|--|----------------------------|
| Diamond-Solid  | 0.1                        | 0.09   | 0.01   | 11.54                      |
|                | 0.5                        | 0.44   | 0.06   | 12.38                      |
|                | 0.9                        | 0.78   | 0.12   | 13.18                      |
|                | 1.3                        | 1.12   | 0.18   | 14.09                      |
| Gyroid-Solid   | 0.1                        | 0.09   | 0.01   | 11.89                      |
|                | 0.5                        | 0.44   | 0.06   | 12.94                      |
|                | 0.9                        | 0.77   | 0.13   | 13.97                      |
|                | 1.3                        | 1.10   | 0.20   | 15.06                      |
| Gyroid-Sheet   | 0.1                        | 0.08   | 0.02   | 16.52                      |
|                | 0.5                        | 0.41   | 0.09   | 17.79                      |
|                | 0.9                        | 0.73   | 0.17   | 19.09                      |
|                | 1.3                        | 1.03   | 0.27   | 20.61                      |

**Table 7**

Heat dissipation of Gyroid-Sheet and Aluminum foam in Ref. [19].

| Temperature Difference (°C) | Heat Dissipated Gyroid Sheet (W) | Heat Dissipated Aluminum Foam (A) (W) | Percentage Difference (%) | Heat Dissipated Aluminum Foam (B) (W) | Percentage Difference (%) |
|-----------------------------|----------------------------------|---------------------------------------|---------------------------|---------------------------------------|---------------------------|
| 45                          | 1.7                              | 1.18                                  | 44.0                      | 1.28                                  | 32.8                      |
| 55                          | 2.1                              | 1.52                                  | 38.6                      | 1.85                                  | 16.7                      |

increasing the solid average surface temperature with increasing heat load (see Fig. 7(d)). In general, the fresh air penetration faces a friction loss resistance due to the no-slip condition, and generated vortices increase resistance nearby the boundary walls around the heat sink. The friction loss resistance is dominant inside the heat sink and is significantly effective in the horizontal layout; whereas the vortices resistance is dominant around the heat sink walls and is significantly effective in the vertical layout. Comparing the Gyroid-sheet heat sink's temperature contours as shown in Fig. 7(d) for the vertical alignment and Fig. 5(c) (Case (2)) for the horizontal alignment, it can be seen that the vertical alignment has a higher temperature in the core of the heat sink due to the impact of the generated vortices on the sides of the heat sink. The generated vortices as explained at the sides of the heat sinks creates an obstacle to the fresh air coming from the bottom decaying their thermal performance. An optimum height could be found by optimizing the height to balance between buoyancy force-induced flow and the entrained flow resistance.

#### 4.3. Influence of thermal radiation

One of the factors that was neglected in the previous simulations is the thermal radiation. In order to determine if the assumption of neglecting thermal radiation is valid, this section tests the influence of radiation on the total heat dissipated in the solid-fluid interface. In this context, radiation is quantified based on the exchanged radiation between surfaces; Surface-To-Surface (S2S) model. The medium between surfaces is assumed to be non-participating since the working medium fluid is air. Radiation was assumed to occur through patches inside the TPMS heat sink, assuming an opaque material that does not transmit any rays through its structure. The emissivity of the heat sink and box was provided in Ref. [73]. Surfaces exposed to the environment are assumed to have a zero thermal radiation resistance because of the large area of the surrounding. The simulation results are summarized in Table 6 (see Table 7).

It is clear from the results in Table 6 that radiation is not a negligible mechanism of heat transfer in buoyancy-induced natural convection in the proposed TPMS-based heat sinks. The radiation contribution in Gyroid-Sheet is larger than the Solid-based heat sinks because of the larger surface area. The radiation contribution accounts for 17% of the total heat transfer for Solid-based TPMS heat sinks, while it is accounting for approximately 23% for the Gyroid-Sheet heat sink. Heat transfer coefficients were obtained including the total heat transfer coefficient ( $\bar{h}_{conv+rad}$ ) from Eq. (20) and the convection heat transfer coefficient ( $\bar{h}_{conv}$ ) from Eq. (21), such that:

$$\bar{h}_{conv+rad} = \frac{\dot{q}_{total}}{A_s(T_{sr} - T_a)} \quad (20)$$

$$\bar{h}_{conv} = \frac{\dot{q}_{conv+cond}}{A_s(T_s - T_a)} \quad (21)$$

where  $\dot{q}_{total}$  is the total heat flux from the interface,  $\dot{q}_{conv+cond}$  is total heat flux excluding the heat dissipated by radiation,  $T_{sr}$  is the surface temperature including the influence of radiation and  $T_s$  is the surface temperature without radiation. Comparing  $\bar{h}_{conv}$  in Fig. 8

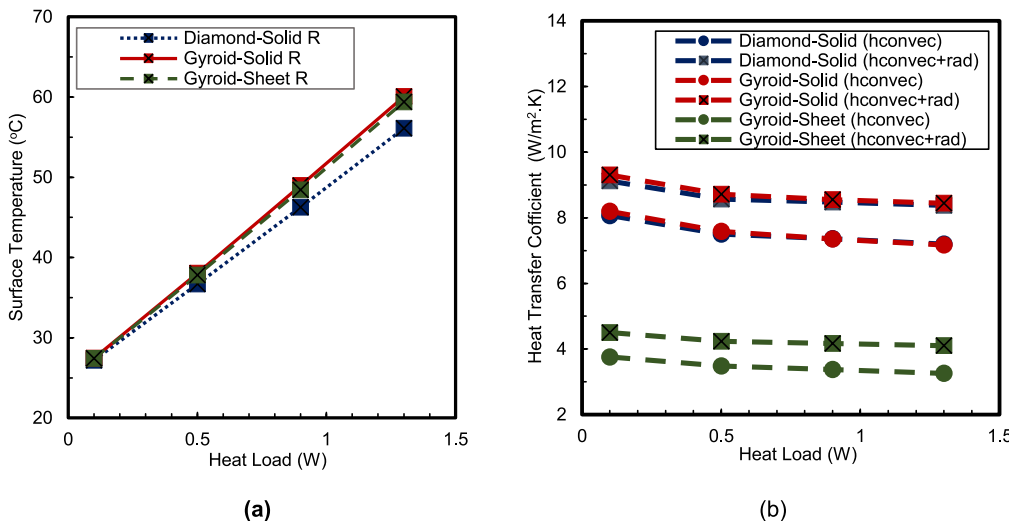


Fig. 8. Radiation effect on thermal performance of the proposed TPMS heat sinks: (a) surface temperature and (b) heat transfer coefficient.

(b) to that in Fig. 3(a) shows an increase of heat transfer coefficient when including radiation. The removal of energy through radiation would result in lowering the surface temperature of radiation shown in Fig. 8(a), thus a higher heat transfer coefficient. Through Fig. 8 (a) it can be observed that the surface temperature of the Gyroid-Sheet heat sink has been reduced significantly which discountenances that Gyroid-Sheet has the worst thermal performance as shown in Fig. 3(a). Interestingly, under the radiation effect, the performance of the Gyroid-Sheet and Gyroid-Solid heat sinks are almost similar and behave better than Diamond-Solid heat sink. This shows the importance of radiation in changing the thermal performance of TPMS-based heat sinks.

#### 4.4. Empirical correlations of TPMS-based heat sinks

The general form of relation between Nusselt and Rayleigh Number in external convection flow is expressed by Eq. (22) from Ref. [73], such that:

$$\bar{Nu} = CRa^a \quad (22)$$

The following correlations are for porous architected TPMS-based heat sinks under free convection when sides and upper surfaces are exposed to the environment (i.e., Case (2)) in their horizontal orientation including radiation effect based on results in Subsection 4.3. The non-dimensional parameters of Nusselt Number ( $\bar{Nu}$ ) and Rayleigh Number ( $Ra$ ) of porous media are defined in Ref. [17] as:

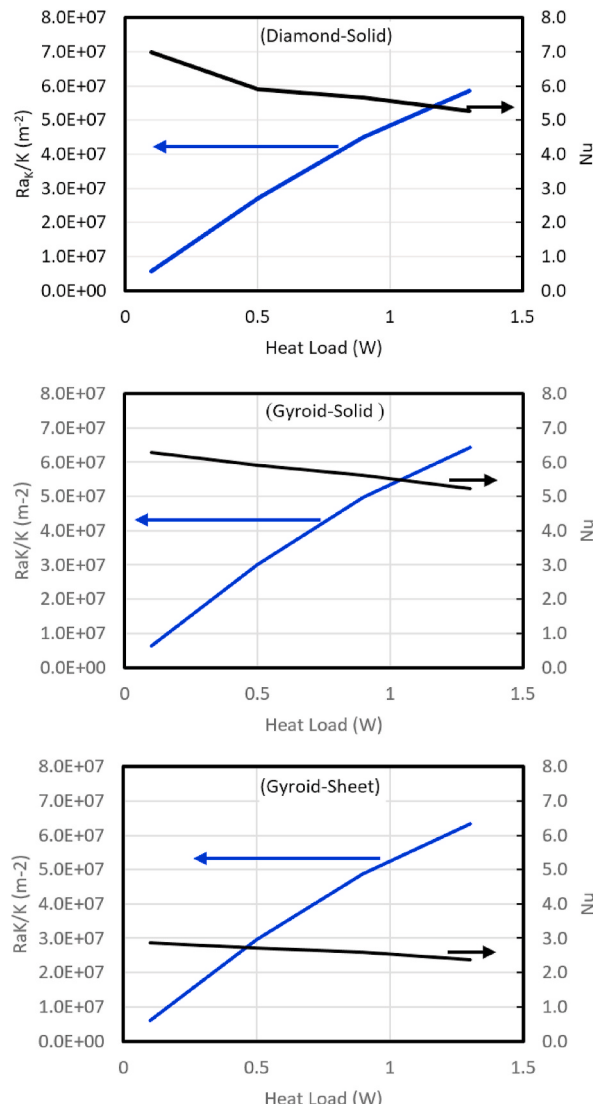


**Fig. 9.** Derived Empirical Equations for case (2) including radiation effect when upper and bottom Boundaries are open (a) Diamond-Solid, (b) Gyroid-Solid and (c) Gyroid-Sheet.

$$\overline{Nu} = \frac{\bar{h}L}{k_e} \quad (23)$$

$$Ra_K = \frac{g\beta(T_s - T_a)KL}{\alpha_e \nu_f} \quad (24)$$

$$\alpha_e = \frac{k_e}{\rho_e c_{pe}} = \frac{k_e}{[\epsilon \rho_f + (1-\epsilon)\rho_{so}] [ec_{pf} + (1-\epsilon)c_{pso}]} \quad (25)$$

where  $L$ ,  $\beta$ ,  $k_e$ ,  $\rho_e$ ,  $\rho_f$ ,  $\rho_{so}$ ,  $c_{pe}$ ,  $c_{pf}$ ,  $c_{pso}$  and  $\alpha_e$  are height, thermal expansion, effective thermal conductivity, effective density, fluid density, solid density, effective specific heat, fluid specific heat, solid specific heat and effective thermal diffusivity, respectively. The parameters  $k_e$ ,  $\rho_f$ ,  $\rho_s$ ,  $c_{pf}$  and  $c_{pso}$  are obtained from the fluid properties.  $K$  and  $\lambda$  are the permeability and porosity of the TPMS structure, respectively. Kim and Vafai [74] expressed the effect of Darcy flow on a vertical plate with a porous medium and found that the thermal boundary layer is larger than the viscous boundary layer when  $Ra_K^{-1/2} \gg Da^{1/2}$  and the viscous boundary layer is larger than the thermal boundary layer when  $Ra_K^{-1/2} \ll Da^{1/2}$ . The expression represented in Eq. (26) follows that in Ref. [17] for metal foam porous media such that:

$$\overline{Nu} \propto Ra_K^{1/2}, \text{ when } Ra_K^{-1/2} \gg Da^{1/2}. \overline{Nu} \propto Ra_K^{1/4} Da^{-1/4}, \text{ when } Ra_K^{-1/2} \ll Da^{1/2} \quad (26)$$

where  $Da = K/L^2$  and  $K$  is the permeability, which has been assumed using the following classical Kozeny-Carman (KC) permeability-porosity relation:

$$K = \frac{\lambda^3}{c(1-\lambda)^2 S^2} \quad (27)$$

where  $c$  is the Kozeny constant approximated to be 5 [75] and  $S$  is the specific surface area calculated as

$$S = \frac{A_s}{V_{so}} \quad (28)$$

where  $V_{so}$  is the solid volume of the structure.  $K$  is found to be  $9.59 \times 10^{-7} m^2$ ,  $1.32 \times 10^{-6} m^2$  and  $2.69 \times 10^{-7} m^2$  for Diamond-Solid, Gyroid-Solid, and Gyroid-Sheet, respectively. Even though  $Ra_K^{-1/2} \gg Da^{1/2}$  found to be valid for all models, the calculated permeability values form Eq (27) are not tested for the TPMS structures. Therefore, the  $Ra_K$  is normalized by the permeability  $K$  in this study. Other studies [76,77] have mentioned that Darcy Number of equal and larger than  $10^{-4}$  can be considerable; however, in this study even Darcy Number is slightly larger but it still holds the restriction of  $Ra_K^{-1/2} \gg Da^{1/2}$ . Regression analysis of computational results shows the predicated empirical correlations for TPMS heat sinks for the Nusselt Number  $\overline{Nu}$  versus the permeability normalized Rayleigh Number  $Ra_K/K$  as shown in equations (29)–(31). The challenges in TPMS porous media are the permeability ( $K$ ) and the interior structure flow resistance. Measuring the permeability for the TPMS structure is not well established yet and all the available models were tested for nanostructured porous media. Fig. 9 show the  $Nu$  and the permeability normalized Ra ( $Ra_K/K$ ) versus the heat load. It shows that increasing the heat load will result in reducing the convection heat transfer coefficient due to the flow resistance and therefore  $Nu$ , on the other hand it will increase the  $Ra_K$  due to the dominant buoyancy force indicating the importance of an orientation comprehensive study for the TPMS structures in free convection.

The permeability ( $K$ ) is a factor that can depend on several parameters such as size, fluid, and the approach of calculation. Permeability can be calculated using several approaches such as using Darcy's Law or the extended Darcy's Law [25,28,76–78]. Determining the correct permeability could assist in understating the behavior of the flow deeply by determining the Darcy Number which expresses the viscous term. As exploited in Fig. 9, the following empirical correlations are derived as a function of both permeability and Rayleigh Number for the investigated TPMS heat sinks under open sides and top surfaces of natural convection flow:

$$\text{Diamond - Solid : } \overline{Nu} = 7.6846 - 0.0003 \left( \frac{Ra_K}{K} \right)^{0.5} \quad (29)$$

$$\text{Gyroid - Solid : } \overline{Nu} = 6.7892 + 0.0002 \left( \frac{Ra_K}{K} \right)^{0.5} \quad (30)$$

$$\text{Gyroid - Sheet : } \overline{Nu} = 3.1297 + 0.00009 \left( \frac{Ra_K}{K} \right)^{0.5} \quad (31)$$

#### 4.5. Comparison to a commercial finned heat sink

A pin-fin heat sink consisting of 18 pin-fins is considered and compared with the performance of the proposed TPMS-based heat sinks. The pin-fin has the same dimensions as the TPMS heat sinks. Also, the enclosure for all models has the same size with opening the top and bottom surfaces to eliminate the difference associated with different types of boundaries. Radiation was included in this study

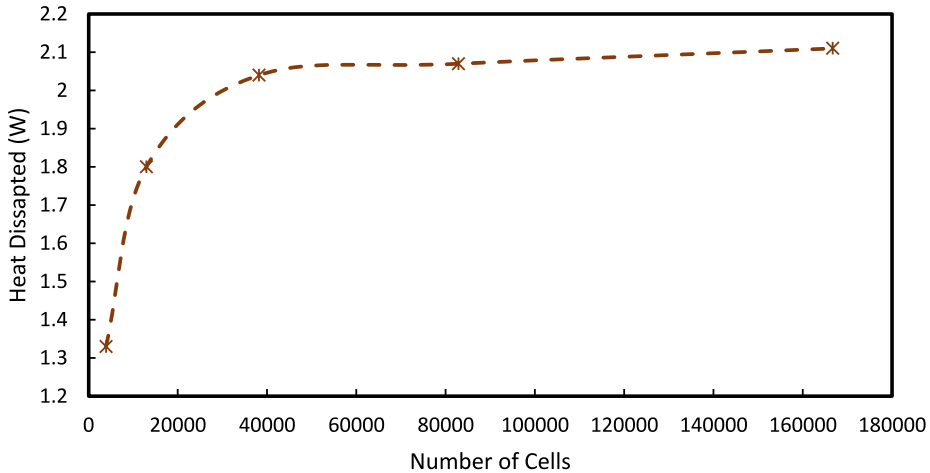


Fig. 10. Mesh sensitivity of pin-fin model.

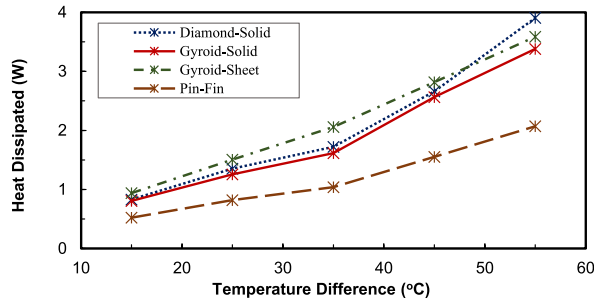


Fig. 11. Amount of heat dissipation by pin-fin heat sink as compared to the current proposed TPMS-based heat sinks.

with having an emissivity of 0.25 for all heat sinks. In order to draw a comparison, a surface temperature is imposed at the interface varying from 40 °C to 80 °C. The mesh sensitivity is performed as shown Fig. 10, as the model become much less sensitive to the finer meshes beyond 80,000 cells, the 86,000 model was chosen in this study.

The effect of changing surface temperature on the amount of heat dissipated from heat sinks is shown in Fig. 11. It is noticed that TPMS-based heat sinks can dissipate up to 48–61% more heat than the commonly-used pin-fin heat sink at 55 °C temperature difference. This is attributed to the high packing density associated with complex flow behavior encountered in TPMS-based heat sinks.

Another comparison was done upon metal foam, in Ref. [19] a study upon Aluminum metal foam heat sink was done experimentally and numerically including radiation effect. The enclosure of the numerical simulation was open from the sides and top surfaces. The size of metal foams chosen for comparison are 250x25 × 18 mm and 250x25x25 mm. Gyroid-Sheet with open sides and top surfaces is chosen for the comparison Table 4. For this type of enclosure, Gyroid-Sheet was used to be compared with the Aluminum foam in the literature. Since the dimension of the Gyroid-Sheet is 22x32 × 22 mm, the heat dissipated of the metal foam taken from article was divided by 10. This will assume the Aluminum foam to have dimensions of 25x25 × 18 mm (A) and 25x25 × 25 mm (B), respectively. Although the comparison is based on assumptions it can be seen that Gyroid-Structure has higher heat dissipation. It also shown less surface temperature compared to the staggered and capped fins [7].

## 5. Conclusions

In this paper and for the first time, the thermal performance and fluid flow of implementing three different TPMS-based designs as heat sinks were studied under natural free convection conditions, which are Diamond-Solid, Gyroid-Solid, and Gyroid-Sheet. As the intended thermal management application of these heat sinks was unspecified, these TPMS heat sinks were investigated under three different environmental boundary conditions or enclosures and two different orientations using CFD. The following key conclusions are drawn from this study:

- Gyroid-Sheet heat sink is found to have superior thermal performance when opening the top and bottom surfaces of the fluid domain enclosure. However, its surface temperature was found to be highest when opening sides and top surfaces of the enclosure.

This was explained by the complex structure of the sheet-networks. Having a larger surface area was opposed by the hydraulic resistance of flow inside the structure which led to a drop in the overall thermal performance.

- TPMS Solid-based heat sinks of the Diamond and Gyroid types are found to have approximately similar trends with the highest thermal performance when opening the top and bottom surfaces of the enclosure and the lowest when opening the bottom surface only of the enclosure.
- The effect of heat sink orientation of both the Diamond-Solid and the Gyroid-Sheet heat sinks were studied where it is found that both structures exhibit a slightly worse thermal performance at their vertical orientation where the longer side is aligned in the vertical direction. Although the buoyancy force found to be enhanced in the larger height, the longer direction acts as a barrier to the fluid flow by inducing vortices.
- Thermal radiation contribution to the overall heat transfer accounted for 17% for the TPMS Solid heat sinks while it is accounted for 23% for the Gyroid-Sheet heat sink. The larger contribution of radiation to the Gyroid-Sheet heat sink has led to enhancing its thermal performance to be similar to the Gyroid-Solid heat sink. Thus, including the radiation effect in natural convection of TPMS-based heat sinks has a significant effect.
- Empirical correlations are developed for the three TPMS heat sinks which relate Nusslet Number ( $\bar{Nu}$ ) to Rayleigh Number ( $Ra$ ).
- Comparing TPMS-based heat sinks with a commonly-used pin-fin heat sink of 15 fins under the same conditions, it was concluded that TPMS heat sinks have 35–50% better thermal performance.

This first study shows the effectiveness of using TPMS geometries as potential novel types of passive heat sinks as compared to commercially available heat sink geometries. Such complicated geometries are becoming a reality thanks to the recent advancements in metallic additive manufacturing where there are much less constraints on the manufacturability of complex heat sink geometries. Future work can focus on studying the effects of porosity, other available TPMS geometries, functional grading of porosity and or TPMS cell size, and hybridization while including different TPMS geometries on the overall performance and optimization of TPMS-based heat sinks.

#### Author statement

Nada Baobaid is graduate student worked on the model and the analysis, Dr. Mohamed Ali is associate professor generated the concept, theory, and the model development and supervise Nada. Dr. Rashid Abu Al-Rub is a professor and Dr. Kamran Khan is an associate professor were the co-advisors, they revised the concept and the manuscript, Dr. Rashid generated the software for the CAD model and Dr. Ali generated the CFD model. All research team members revised and responded to the reviewers comments. All team are members of the Advanced Digital & Additive Manufacturing (ADAM) Center at Khalifa University, Abu Dhabi, UAE.

#### Declaration of competing interest

The authors declare that they have no known competing financial interests or personal relationships that could have appeared to influence the work reported in this paper.

#### Acknowledgement

This work is based upon work supported by the Khalifa University of Science and Technology under Awards No. CIRA-2018-51 and No. RCII-2019-003.

#### Appendix A. Supplementary data

Supplementary data to this article can be found online at <https://doi.org/10.1016/j.csite.2022.101944>.

#### References

- [1] S.S. Haghghi, H.R. Goshayeshi, M.R. Safaei, Natural convection heat transfer enhancement in new designs of plate-fin based heat sinks, *Int. J. Heat Mass Tran.* 125 (2018) 640–647, <https://doi.org/10.1016/j.ijheatmasstransfer.2018.04.122>.
- [2] S. Zulk, T. Koneke, A. Mertens, Analytical Modeling of Plate Fin Heat Sinks for Natural Convection Cooling in Power Electronics, 2016, <https://doi.org/10.1109/VPPC.2016.7791618>.
- [3] S.W. Pua, K.S. Ong, K.C. Lai, M.S. Naghavi, Natural and forced convection heat transfer coefficients of various finned heat sinks for miniature electronic systems, *Proc. Inst. Mech. Eng. Part A J. Power Energy* 233 (2) (2019) 249–261, <https://doi.org/10.1177/0957650918784420>.
- [4] S. Feng, M. Shi, H. Yan, S. Sun, F. Li, T.J. Lu, Natural convection in a cross-fin heat sink, *Appl. Therm. Eng.* 132 (2018) 30–37, <https://doi.org/10.1016/j.applthermaleng.2017.12.049>.
- [5] E.A.M. Elshafei, Natural convection heat transfer from a heat sink with hollow/perforated circular pin fins, in: 2010 3rd International Conference on Thermal Issues in Emerging Technologies, Theory and Applications - Proceedings, ThETA3 2010, 2010, pp. 185–193, <https://doi.org/10.1109/THETA.2010.5766397>.
- [6] A.M.E. Arefin, Thermal analysis of modified pin fin heat sink for natural convection, in: 2016 5th International Conference on Informatics, Electronics and Vision, ICIEV 2016, 2016, pp. 1–5, <https://doi.org/10.1109/ICIEV.2016.7759986>.
- [7] H. Mousavi, A.A. Rabienataj Darzi, M. Farhadi, M. Omidi, A novel heat sink design with interrupted, staggered and capped fins, *Int. J. Therm. Sci.* 127 (2018) 312–320, <https://doi.org/10.1016/j.ijthermalsci.2018.02.003>. January 2017.
- [8] M.I. Hasan, H.L. Tbena, Enhancing the cooling performance of micro pin fin heat sink by using the phase change materials with different configurations, in: International Conference on Advances in Sustainable Engineering and Applications, ICASEA 2018 - Proceedings, 2018, pp. 205–209, <https://doi.org/10.1109/ICASEA.2018.8370982>.

- [9] L. Micheli, K.S. Reddy, T.K. Mallick, Experimental comparison of micro-scaled plate-fins and pin-fins under natural convection, *Int. Commun. Heat Mass Tran.* 75 (2016) 59–66, <https://doi.org/10.1016/j.icheatmasstransfer.2016.03.023>.
- [10] M.I. Hasan, Study of microchannel heat sink performance with expanded microchannels and nanofluid, *J. Al-Qadisiya Eng. Sci.* 2016 (2016) no. January.
- [11] S.T. Kadam, R. Kumar, Twenty first century cooling solution: microchannel heat sinks, *Int. J. Therm. Sci.* 85 (2014) 73–92, <https://doi.org/10.1016/j.ijthermalsci.2014.06.013>. Elsevier Masson SAS.
- [12] D.B. Tuckerman, R.F.W. Pease, High-performance heat sinking for VLSI, *IEEE Electron. Device Lett.* EDL-2 (5) (1981) 126–129, <https://doi.org/10.1109/EDL.1981.25367>.
- [13] T. Qiu, D. Wen, W. Hong, Y. Liu, Heat transfer performance of a porous copper micro-channel heat sink, *J. Therm. Anal. Calorim.* 139 (2) (2020) 1453–1462, <https://doi.org/10.1007/s10973-019-08547-4>.
- [14] M. Mazur, M. Leary, M. McMillan, S. Sun, D. Shidid, M. Brandt, Mechanical properties of Ti6Al4V and AlSi12Mg lattice structures manufactured by Selective Laser Melting (SLM), in: *Laser Additive Manufacturing: Materials, Design, Technologies, and Applications*, 2017, pp. 119–161.
- [15] O. Al-Ketan, R. Rowshan, R.K. Abu Al-Rub, Topology-mechanical property relationship of 3D printed strut, skeletal, and sheet based periodic metallic cellular materials, *Addit. Manuf.* 19 (2018) 167–183, <https://doi.org/10.1016/j.addma.2017.12.006>.
- [16] C.Y. Zhao, Review on thermal transport in high porosity cellular metal foams with open cells, *Int. J. Heat Mass Tran.* 55 (13–14) (2012) 3618–3632, <https://doi.org/10.1016/j.ijheatmasstransfer.2012.03.017>.
- [17] A. Bhattacharya, R.L. Mahajan, Metal foam and finned metal foam heat sinks for electronics cooling in buoyancy-induced convection, *J. Electron. Packag. Trans. ASME* 128 (3) (2006) 259–266, <https://doi.org/10.1115/1.2229225>.
- [18] M.S. Phankumar, R.L. Mahajan, Non-Darcy natural convection in high porosity metal foams, *Int. J. Heat Mass Tran.* 45 (18) (2002) 3781–3793, [https://doi.org/10.1016/S0017-9310\(02\)00089-3](https://doi.org/10.1016/S0017-9310(02)00089-3).
- [19] S. De Schampheleire, K. De Kerpel, P. De Jaeger, H. Huisseune, B. Ameel, M. De Paepe, Buoyancy driven convection in open-cell metal foam using the volume averaging theory, *Appl. Therm. Eng.* 79 (2015) 225–233, <https://doi.org/10.1016/j.applthermaleng.2015.01.019>.
- [20] S. De Schampheleire, et al., Experimental study of buoyancy-driven flow in open-cell aluminium foam heat sinks, *Appl. Therm. Eng.* 59 (1–2) (2013) 30–40, <https://doi.org/10.1016/j.applthermaleng.2013.05.010>.
- [21] M. Billiet, S. De Schampheleire, H. Huisseune, M. De Paepe, Influence of orientation and radiative heat transfer on aluminum foams in buoyancy-induced convection, *Materials* 8 (10) (2015) 6792–6805, <https://doi.org/10.3390/ma8105340>.
- [22] S. Feng, F. Li, F. Zhang, T.J. Lu, Natural convection in metal foam heat sinks with open slots, *Exp. Therm. Fluid Sci.* 91 (2018) 354–362, <https://doi.org/10.1016/j.expthermflusci.2017.07.010>.
- [23] Z.G. Qu, H.J. Xu, T.S. Wang, W.Q. Tao, T.J. Lu, Thermal transport in metallic porous media, in: *Heat Transfer - Engineering Applications*, 2011.
- [24] C.Y. Zhao, T.J. Lu, H.P. Hodson, Natural convection in metal foams with open cells, *Int. J. Heat Mass Tran.* 48 (12) (2005) 2452–2463, <https://doi.org/10.1016/j.ijheatmasstransfer.2005.01.002>.
- [25] J.Y. Ho, K.C. Leong, T.N. Wong, Experimental and numerical investigation of forced convection heat transfer in porous lattice structures produced by selective laser melting, *Int. J. Therm. Sci.* 137 (2019) 276–287, <https://doi.org/10.1016/j.ijthermalsci.2018.11.022>.
- [26] J. Tian, et al., The effects of topology upon fluid-flow and heat-transfer within cellular copper structures, *Int. J. Heat Mass Tran.* 47 (14–16) (2004) 3171–3186, <https://doi.org/10.1016/j.ijheatmasstransfer.2004.02.010>.
- [27] T. Kim, H.P. Hodson, T.J. Lu, Fluid-flow and endwall heat-transfer characteristics of an ultralight lattice-frame material, *Int. J. Heat Mass Tran.* 47 (6–7) (2004) 1129–1140, <https://doi.org/10.1016/j.ijheatmasstransfer.2003.10.012>.
- [28] A. Chaudhari, P. Ekade, S. Krishnan, Experimental investigation of heat transfer and fluid flow in octet-truss lattice geometry, *Int. J. Therm. Sci.* 143 (2019) 64–75, <https://doi.org/10.1016/j.ijthermalsci.2019.05.003>. April.
- [29] P. Ekade, S. Krishnan, Fluid flow and heat transfer characteristics of octet truss lattice geometry, *Int. J. Therm. Sci.* 137 (2019) 253–261, <https://doi.org/10.1016/j.ijthermalsci.2018.11.031>. April 2018.
- [30] T. Wen, J. Tian, T.J. Lu, D.T. Queheillalt, H.N.G. Wadley, Forced convection in metallic honeycomb structures, *Int. J. Heat Mass Tran.* 49 (19–20) (2006) 3313–3324, <https://doi.org/10.1016/j.ijheatmasstransfer.2006.03.024>.
- [31] M. Ozsipahi, A. Subasi, H. Gunes, B. Sahin, Numerical investigation of hydraulic and thermal performance of a honeycomb heat sink, *Int. J. Therm. Sci.* 134 (2018) 500–506, <https://doi.org/10.1016/j.ijthermalsci.2018.07.034>. July.
- [32] X. Wang, M. Chen, D. Tate, H. Rahimi, S. Zhang, Numerical investigation on hydraulic and thermal characteristics of micro latticed pin fin in the heat sink, *Int. J. Heat Mass Tran.* 149 (2020), 119157, <https://doi.org/10.1016/j.ijheatmasstransfer.2019.119157>.
- [33] W. Li, G. Yu, Z. Yu, Bioinspired heat exchangers based on triply periodic minimal surfaces for supercritical CO<sub>2</sub> cycles, *Appl. Therm. Eng.* 179 (2020), 115686, <https://doi.org/10.1016/j.applthermaleng.2020.115686>. February.
- [34] D. Shamvedi, O.J. McCarthy, E. O'Donoghue, C. Danilenhoff, P. O'Leary, R. Raghavendra, 3D Metal printed heat sinks with longitudinally varying lattice structure sizes using direct metal laser sintering, *Virtual Phys. Prototyp.* 13 (4) (2018) 301–310, <https://doi.org/10.1080/17452759.2018.1479528>.
- [35] K.J. Malone, K.D. Fink, T.A. Schaedler, J.A. Kolodziejska, A.J. Jacobsen, C.S. Roper, Multifunctional heat exchangers derived from three-dimensional micro-lattice structures, *Int. J. Heat Mass Tran.* 55 (9–10) (2012) 2486–2493, <https://doi.org/10.1016/j.ijheatmasstransfer.2012.01.011>.
- [36] J.Y. Ho, K.C. Leong, T.N. Wong, Additively-manufactured metallic porous lattice heat exchangers for air-side heat transfer enhancement, *Int. J. Heat Mass Tran.* 150 (2020), <https://doi.org/10.1016/j.ijheatmasstransfer.2019.119262>.
- [37] K.N. Son, J.A. Weibel, V. Kumaresan, S.V. Garimella, Design of multifunctional lattice-frame materials for compact heat exchangers, *Int. J. Heat Mass Tran.* 115 (2017) 619–629, <https://doi.org/10.1016/j.ijheatmasstransfer.2017.07.073>.
- [38] D. Bhatia, C.A. Penick, L.A. Ferry, C. Lee, Classification and selection of cellular materials in mechanical design: engineering and biomimetic approaches, *Designs* 3 (1) (2019) 1–31, <https://doi.org/10.3390/designs3010019>.
- [39] A.H. Schoen, Reflections concerning triply-periodic minimal surfaces, *Interface Focus* 2 (5) (2012) 658–668, <https://doi.org/10.1098/rsfs.2012.0023>.
- [40] G. Savio, S. Rosso, R. Meneghelli, G. Concheri, Geometric modeling of cellular materials for additive manufacturing in biomedical field: a review, *Appl. Bionics Biomechanics* 2018 (2018), <https://doi.org/10.1155/2018/1654782>.
- [41] D.J. Yoo, Porous scaffold design using the distance field and triply periodic minimal surface models, *Biomaterials* 32 (31) (2011) 7741–7754, <https://doi.org/10.1016/j.biomaterials.2011.07.019>.
- [42] J. Feng, J. Fu, C. Shang, Z. Lin, B. Li, Sandwich panel design and performance optimization based on triply periodic minimal surfaces, *CAD Comput. Aided Des.* 115 (2019) 307–322, <https://doi.org/10.1016/j.cad.2019.06.007>.
- [43] O. Al-Ketan, R. Rezgui, R. Rowshan, H. Du, N.X. Fang, R.K. Abu Al-Rub, Microarchitected stretching-dominated mechanical metamaterials with minimal surface topologies, *Adv. Eng. Mater.* 20 (9) (2018), <https://doi.org/10.1002/adem.201800029>.
- [44] G. Savio, R. Meneghelli, G. Concheri, Design of variable thickness triply periodic surfaces for additive manufacturing, *Prog. Addit. Manuf.* 4 (3) (2019) 281–290, <https://doi.org/10.1007/s40964-019-00073-x>.
- [45] S.J. Yeo, M.J. Oh, P.J. Yoo, Structurally controlled cellular architectures for high-performance ultra-lightweight materials, *Adv. Mater.* 31 (34) (2019), <https://doi.org/10.1002/adma.201803670>.
- [46] L. Li, et al., Early osteointegration evaluation of porous Ti6Al4V scaffolds designed based on triply periodic minimal surface models, *J. Orthop. Transl.* 19 (2019) 94–105, <https://doi.org/10.1016/j.jot.2019.03.003>.
- [47] L.Y. Zhu, et al., Design and biomechanical characteristics of porous meniscal implant structures using triply periodic minimal surfaces, *J. Transl. Med.* 17 (1) (2019), <https://doi.org/10.1186/s12967-019-1834-2>.
- [48] S. Tan, J. Gu, S.C. Han, D.W. Lee, K. Kang, Design and fabrication of a non-clogging scaffold composed of semi-permeable membrane, *Mater. Des.* 142 (2018) 229–239, <https://doi.org/10.1016/j.matedes.2018.01.033>.
- [49] O. Al-Ketan, M. Pelanconi, A. Ortona, R.K. Abu Al-Rub, Additive manufacturing of architected catalytic ceramic substrates based on triply periodic minimal surfaces, *J. Am. Ceram. Soc.* 102 (10) (2019) 6176–6193, <https://doi.org/10.1111/jace.16474>.

- [50] D.W. Abueidda, I. Jasiuk, N.A. Sobh, Acoustic band gaps and elastic stiffness of PMMA cellular solids based on triply periodic minimal surfaces, *Mater. Des.* 145 (2018) 20–27, <https://doi.org/10.1016/j.matdes.2018.02.032>.
- [51] N. Thomas, N. Sreedhar, O. Al-Ketan, R. Rowshan, R.K. Abu Al-Rub, H. Arafat, 3D printed triply periodic minimal surfaces as spacers for enhanced heat and mass transfer in membrane distillation, *Desalination* 443 (2018) 256–271, <https://doi.org/10.1016/j.desal.2018.06.009>.
- [52] T. Femmer, A.J.C. Kuehne, M. Wessling, Estimation of the structure dependent performance of 3-D rapid prototyped membranes, *Chem. Eng. J.* 273 (2015) 438–445, <https://doi.org/10.1016/j.cej.2015.03.029>.
- [53] T. Femmer, A.J.C. Kuehne, J. Torres-Rendon, A. Walther, M. Wessling, Print your membrane: rapid prototyping of complex 3D-PDMS membranes via a sacrificial resist, *J. Memb. Sci.* 478 (2015) 12–18, <https://doi.org/10.1016/j.memsci.2014.12.040>.
- [54] O. Al-Ketan, M. Ali, M. Khalil, R. Rowshan, K.A. Khan, R.K. Abu Al-Rub, Forced convection computational fluid dynamics analysis of architected and three-dimensional printable heat sinks based on triply periodic minimal surfaces, *J. Therm. Sci. Eng. Appl.* 13 (2) (2021).
- [55] Z.A. Qureshi, S.A.B. Al-Omari, E. Elnajjar, O. Al-Ketan, R. Abu Al-Rub, Using triply periodic minimal surfaces (TPMS)-based metal foams structures as skeleton for metal-foam-PCM composites for thermal energy storage and energy management applications, *Int. Commun. Heat Mass Tran.* 124 (2021), 105265, <https://doi.org/10.1016/j.icheatmastransfer.2021.105265>. April.
- [56] Z.A. Qureshi, E. Elnajjar, O. Al-Ketan, R. Abu Al-Rub, S.B. Al-Omari, Heat transfer performance of a finned metal foam-phase change material (FMF-PCM) system incorporating triply periodic minimal surfaces (TPMS), *Int. J. Heat Mass Tran.* 170 (2021), 121001, <https://doi.org/10.1016/j.ijheatmasstransfer.2021.121001>.
- [57] Z.A. Qureshi, S.A.B. Al Omari, E. Elnajjar, F. Mahmoud, O. Al-Ketan, R.A. Al-Rub, Thermal characterization of 3D-Printed lattices based on triply periodic minimal surfaces embedded with organic phase change material, *Case Stud. Therm. Eng.* 27 (2021), 101315, <https://doi.org/10.1016/j.csite.2021.101315>. August.
- [58] X. Hu, X. Gong, Experimental study on the thermal response of PCM-based heat sink using structured porous material fabricated by 3D printing, *Case Stud. Therm. Eng.* 24 (2021), 100844, <https://doi.org/10.1016/j.csite.2021.100844>. January.
- [59] O. Al-Ketan, R.K. Abu Al-Rub, Multifunctional mechanical metamaterials based on triply periodic minimal surface lattices, *Adv. Eng. Mater.* 21 (10) (2019), <https://doi.org/10.1002/adem.201900524>.
- [60] T. Wu, B. Ozpineci, C. Ayers, Genetic algorithm design of a 3D printed heat sink, in: Conference Proceedings - IEEE Applied Power Electronics Conference and Exposition - APEC 2016-May, 2016, pp. 3529–3536, <https://doi.org/10.1109/APEC.2016.7468376>.
- [61] M. Fasano, et al., Passive heat transfer enhancement by 3D printed Pitot tube based heat sink, *Int. Commun. Heat Mass Tran.* 74 (2016) 36–39, <https://doi.org/10.1016/j.icheatmastransfer.2016.03.012>.
- [62] A. Radwan, S. Ookawara, S. Mori, M. Ahmed, Uniform cooling for concentrator photovoltaic cells and electronic chips by forced convective boiling in 3D-printed monolithic double-layer microchannel heat sink, *Energy Convers. Manag.* 166 (May) (2018) 356–371, <https://doi.org/10.1016/j.enconman.2018.04.037>.
- [63] Y.S. See, K.C. Leong, Heat transfer study of 3 dimensional printed air-cooled heat sinks, in: 13th International Conference on Heat Transfer, Fluid Mechanics and Thermodynamics, 2017, pp. 852–859 [Online]. Available: <https://repository.up.ac.za/handle/2263/62351>.
- [64] J.Y. Ho, K.K. Wong, K.C. Leong, T.N. Wong, Convective heat transfer performance of airfoil heat sinks fabricated by selective laser melting, *Int. J. Therm. Sci.* 114 (2017) 213–228, <https://doi.org/10.1016/j.ijthermalsci.2016.12.016>.
- [65] K.K. Wong, J.Y. Ho, K.C. Leong, T.N. Wong, Fabrication of heat sinks by Selective Laser Melting for convective heat transfer applications, *Virtual Phys. Prototyp.* 11 (3) (2016) 159–165, <https://doi.org/10.1080/17452759.2016.1211849>.
- [66] J.Y. Ho, K.K. Wong, K.C. Leong, Saturated pool boiling of FC-72 from enhanced surfaces produced by Selective Laser Melting, *Int. J. Heat Mass Tran.* 99 (2016) 107–121, <https://doi.org/10.1016/j.ijheatmasstransfer.2016.03.073>.
- [67] K.K. Wong, K.C. Leong, Saturated pool boiling enhancement using porous lattice structures produced by Selective Laser Melting, *Int. J. Heat Mass Tran.* 121 (2018) 46–63, <https://doi.org/10.1016/j.ijheatmasstransfer.2017.12.148>.
- [68] J. Y. Ho and K. C. Leong, "Filmwise Condensation on Micro-Fin Surfaces Produced by," pp. 85–90.
- [69] O. Al-Ketan, R.K. Abu Al-Rub, MSLattice: a free software for generating uniform and graded lattices based on triply periodic minimal surfaces, *Mater. Des. Process. Commun.* (2020), <https://doi.org/10.1002/mdp2.205>, 3.
- [70] Simcenter STAR-CCM+, "STAR-CCM." Siemens PLM Software, 2018.
- [71] Simcenter STAR-CCM+, Siemens PLM Software, 2018.
- [72] JMatPro the Materials Property Simulation Package, Senter Software Ltd, Surrey Technology Center, UK, 2014.
- [73] Y. Ma, Z. He, X. Peng, Z. Xing, Experimental investigation of the discharge valve dynamics in a reciprocating compressor for trans-critical CO<sub>2</sub> refrigeration cycle, *Appl. Therm. Eng.* 32 (1) (2012) 13–21, <https://doi.org/10.1016/j.applthermaleng.2011.03.022>.
- [74] S.J. Kim, K. Vafai, Analysis of natural convection about a vertical plate embedded in a porous medium, *Int. J. Heat Mass Tran.* 32 (4) (1989) 665–677, [https://doi.org/10.1016/0017-9310\(89\)90214-7](https://doi.org/10.1016/0017-9310(89)90214-7).
- [75] P. Xu, B. Yu, Developing a new form of permeability and Kozeny-Carman constant for homogeneous porous media by means of fractal geometry, *Adv. Water Resour.* 31 (1) (2008) 74–81, <https://doi.org/10.1016/j.advwatres.2007.06.003>.
- [76] S. Goyal, R.G. Larson, C.J. Aloisio, Prediction of impact forces for shock-cushioning elastomer-pad design, in: Biomedical Sciences Instrumentation 35, 1999, pp. 15–21, <https://doi.org/10.2495/CMEM990141>.
- [77] N. Kladias, V. Prasad, Natural convection in horizontal porous layers: effects of Darcy and Prandtl numbers, in: American Society of Mechanical Engineers, Heat Transfer Division, (Publication) HTD 96, 1988, pp. 593–603, <https://doi.org/10.1115/1.3250807>. November 1989.
- [78] F. Gharibi, M. Ashrafihaadeh, "Darcy and inertial fluid flow simulations in porous media using the non-orthogonal central moments lattice Boltzmann method," *J. Petrol. Sci. Eng.* 194 (May, 2020) <https://doi.org/10.1016/j.petrol.2020.107572>.